Subseasonal drivers of extreme fire weather in Australia and its prediction in ACCESS-S1 during spring and summer

Andrew G. Marshall[1]

Paul A. Gregory[2]

Catherine O. de Burgh-Day[2]

Morwenna Griffiths[2]

1. Bureau of Meteorology, Hobart, Tasmania, Australia

2. Bureau of Meteorology, Docklands, Victoria, Australia

Wednesday 9 June 2021

Corresponding Author: Andrew G. Marshall

Bureau of Meteorology

Hobart, Tasmania, Australia

Andrew.Marshall@bom.gov.au

Abstract

We assess the ability of the Bureau of Meteorology's ACCESS-S1 dynamical forecast system to simulate and predict extreme fire weather over Australia during austral spring (SON) and summer (DJF) on subseasonal timescales. Specifically, we focus on the roles of the El Niño – Southern Oscillation (ENSO), Indian Ocean Dipole (IOD), Southern Annular Mode (SAM), Madden-Julian Oscillation (MJO), and two modes of persistent high-pressure in the Australian region characterised as (i) split-flow blocking highs and (ii) subtropical ridge Tasman highs (STRH). The observed likelihood of extreme fire weather increases over most of Australia in association with El Niño, the positive IOD, negative SAM and low split-flow blocking, in both seasons. These increases are generally largest in SON over the southeast. Notable increases in the likelihood of extreme fire weather also occur north of 30°S during low STRH activity, and over the southeast during MJO phase 3. Using retrospective forecasts at lead times of 2-3 weeks for the period 1990-2012, we show that ACCESS-S1 simulates reasonably well the observed modulation of extreme weekly-mean fire weather by each climate driver, however the simulated changes in probabilities are often weaker than those observed. Each climate driver plays an important role in providing predictive skill for regions where ACCESS-S1 captures a high likelihood of experiencing extreme fire weather conditions. The results of this study highlight windows of forecast opportunity during active climate driver phases that can be useful to regional users in fire management, emergency services, health, national park management, and the agriculture and energy sectors.

1 Introduction

Much of Australia has experienced an increase in extreme fire weather over the last few decades due to warmer and drier conditions (CSIRO and Bureau of Meteorology 2015, 2020). Extreme fire weather days have become more frequent and the extratropical Australian bushfire season has extended further into spring and autumn (Clarke et al. 2013, Dowdy 2018). Continued warming and drying in climate projections over the 21st century will lead to harsher fire weather for southern and eastern Australia (CSIRO and Bureau of Meteorology 2015), including many of the areas devastated by fire activity during the recent 2018-2019 and 2019-2020 bushfire seasons.

The 2019-2020 season was the worst fire season on record for Australia. During spring, dangerous fire weather across Australia led to several large wildfires that flared in early September. These occurred during hot, dry and windy conditions suitable for fire spread (Bradstock 2010). Fires continued to burn into November, during which several lives were lost and hundreds of homes were destroyed. Over 1.9 million hectares had been burnt by the end of November 2019, much of which occurred in eastern New South Wales (1.65 million hectares) and eastern Queensland (220,000 hectares) (Bureau of Meteorology, 2019c), including areas of Queensland not usually subject to dangerous fire weather. Each Australian State and the Northern Territory reported damaging fire activity during the season. Smoke generated by the fires impacted both surface air quality and global atmospheric composition as it drifted across the Pacific Ocean and ascended to stratospheric heights of more than 30 km, previously matched by the Mt. Pinatubo eruption in 1991 (NASA 2020, Khaykin et al. 2020, Ohneiser et al. 2020).

Below-average rainfall since 2017 and above-average daytime temperatures in 2019 created low soil moisture over much of Australia (leading to dry fuels), resulting in high fire danger from early spring 2019 (Bureau of Meteorology, 2019b). These antecedent factors combined with modes of subseasonal to seasonal climate variability, or 'climate drivers', to exacerbate the warm and dry conditions over many parts of the country. In the second half of 2019, a strong positive Indian Ocean Dipole (IOD; Saji et al. 1999, Wang et al. 2020) promoted reduced rainfall and warmer conditions across Australia (e.g. Risbey et al. 2009). Then, during October and November 2019, a prolonged negative phase of the Southern Annular Mode (SAM, e.g. Trenberth 1979) enhanced the dry, warm and windy environment of New South Wales and Queensland, following an unusually strong Sudden Stratospheric Warming event over Antarctica (SSW; Scherhag 1952, Hendon et al. 2019, Lim et al. 2020). These dangerous fire weather conditions continued into December, which was the warmest December on record for Australia as a whole and for all mainland States except Victoria (Bureau of Meteorology, 2020). The accumulated fire danger for that month was also the highest recorded for Australia as a whole, as new records were set across large areas of the country. Fire weather conditions generally eased back from record levels in the second half of January 2020 as the positive Indian Ocean Dipole and the negative Southern Annular Mode broke down (Bureau of Meteorology, 2020).

Just one year prior, during the summer of 2018-2019, significant fires had also affected parts of eastern Queensland (November-December), southern Tasmania and eastern Victoria (January-February), and northeast New South Wales and southwest Western Australia (February). For Tasmania, over 178,000 ha were burnt – representing 2.6 per cent of the state – including 14 per cent of globally significant very tall wet eucalypt forests and

91 a total of 95,000 ha (6%) of the Tasmanian Wilderness World Heritage Area (AFAC 2019),
92 as the air quality deteriorated across the state due to the high concentrations of surface
93 smoke (Bureau of Meteorology, 2019a).

94 The widespread and devastating impacts of the recent 2018-2019 and 2019-2020
95 Australian bushfire seasons highlight the importance of understanding climatic factors that
96 contribute to extreme fire danger, including large-scale climate drivers active at the time.
97 Previous work has linked elevated fire weather conditions in Australia to the El Niño–
98 Southern Oscillation (ENSO; e.g. Love and Downey 1986, Williams and Karoly 1999,
99 Williams et al 2001, Lucas et al. 2007, Dowdy 2018, Harris and Lucas 2019), IOD (e.g.
100 Harris and Lucas 2019) and SAM (e.g. Harris and Lucas 2019, Lim et al. 2019), including
101 for fire weather extremes (Williams and Karoly 1999, Harris and Lucas 2019).

102 We build on these previous studies by providing a comprehensive assessment of the
103 impacts of six key drivers of Australian subseasonal climate variability on extreme fire
104 weather, and their depiction and prediction in the Bureau of Meteorology's seasonal climate
105 forecast system ACCESS-S1 (Hudson et al. 2017). This assessment is important for
106 contributing to (i) the development and understanding of operational forecasts of extreme
107 fire danger by identifying the role of each climate driver, and (ii) international research
108 efforts on improving dynamical prediction on the subseasonal timescale (e.g. Brunet et al.
109 2010). We assess fire weather using the McArthur forest fire danger index (FFDI;
110 McArthur 1967), which is currently the most commonly used measure for examining fire
111 weather conditions in Australia, and the index used by the Australian Bureau of
112 Meteorology (BoM) for communicating the risk of fire danger to Australian fire
113 management authorities. As a key tool for assessing fire danger in Australia, the FFDI has

been shown to provide a useful indication of fire weather based predominantly on meteorological variables and can be used as a basis for issuing regional warnings and fire bans (e.g., Lucas 2010, Dowdy et al. 2018, and Harris and Lucas 2019).

We define extreme fire weather to be weekly mean FFDI above the 90th percentile (the upper decile), and we assess impacts of the Madden-Julian Oscillation (MJO, e.g. Madden and Julian 1994) and two modes of persistent anticyclone in the Australian region (e.g. Marshall et al. 2014b) in addition to the ENSO, IOD and SAM. These climate drivers can influence fire extremes through their influence on important weather variables such as extreme temperature, rainfall and wind (e.g. Kenyon and Hegerl 2008, Arblaster and Alexander 2012, Marshall et al. 2014b, White et al. 2014, Marshall et al. 2020). Given our ability to predict these climate drivers on timescales from weeks to seasons ahead (e.g. Hudson et al. 2017), improved understanding of their impacts on extreme fire weather conditions in Australia will help with predicting the fire potential across the country each year and thus be of great benefit to many sectors including health, agriculture, energy, national park and emergency management.

The focus of this study is on the extratropical Australian bushfire season incorporating austral spring (September to November; SON) and summer (December to February; DJF). We note that all the climate drivers examined here exhibit strong relationships to extreme fire behaviour year-round; their influences during the northern/tropical Australian dry season (May to October) is a topic for future work. Section 2 of this paper provides a brief description of the ACCESS-S1 dynamical forecast system, the retrospective forecasts ('hindcasts') and observational datasets and methods of analysis. The following sections provide an assessment of the capability of ACCESS-S1 to depict (Section 3) and predict

(Section 4) extreme weekly mean fire weather conditions over Australia, highlighting the role of each climate driver. We will also highlight areas where further model development and improvement may be required. A summary and conclusions are presented in Section 5.

2 Data and Methods

a) Observed fire weather using the Forest Fire Danger Index

We represent extreme fire weather in observations using a daily gridded FFDI dataset for Australia produced and maintained by Climate Services at the Bureau of Meteorology and described by Lucas (2010) and Dowdy (2018). Our FFDI formulation is based on Noble et al. (1980) but rearranged to improve computational efficiency for large gridded datasets. It combines daily observations of 2 m maximum temperature (T), 2 m relative humidity (RH) calculated from vapour pressure at 0600 UTC (near the time of maximum temperature), 10 m wind speed at 0600 UTC (v), and a drought factor (DF) that represents an accumulated deficit in fuel moisture based on antecedent daily rainfall totals and 2 m maximum temperature (equation 1).

$$FFDI = \exp(0.0338\,T - 0.0345\,RH + 0.0243\,v + 0.243147) \,.\, DF^{0.987} \quad (1)$$

The temperature, vapour pressure and rainfall data are from the Australian Water Availability Project (AWAP; Jones et al. 2009), and the wind speed data are from the 6-

160 hourly NCEP–NCAR reanalysis (NNR1; Kalnay et al. 1996). The AWAP analyses are an
161 optimum interpolation of all available daily station observations (600-800 stations daily)
162 that provide good coverage across the continent except in parts of the Australian outback
163 including the Gibson Desert (central Western Australia), Great Victorian Desert (Western
164 Australia and South Australia) and Simpson Desert (Northern Territory, South Australia
165 and Queensland) where caution needs to be used (Jones et al. 2009). Thus, our key focus
166 is on the temperate and subtropical regions of Australia, where the FFDI is also most widely
167 used. For calculating the FFDI, the NNR1 wind speed data is interpolated to the 0.05°
168 AWAP grid and calibrated (quantile-quantile matched; Bureau of Meteorology 2019d) to
169 the wind speed produced at 0600 UTC by the Bureau of Meteorology's operational
170 numerical weather prediction model. The drought factor, a number between 0 and 10, is
171 calculated using the Keetch–Byram drought index (KBDI; Keetch and Byram 1968), as
172 described by Griffiths (1999) and Finkele et al. (2006). Further details of the KBDI and
173 FFDI are also provided by Lucas (2010), Dowdy et al. (2018) and Harris and Lucas (2019).
174 The observed FFDI data are available on a 0.05° horizontal grid. We calculate 7-day means
175 from the daily FFDI data for the period 1990 to 2012 (the ACCESS-S1 hindcast period),
176 and anomalies relative to climatology for the climate driver indices (detailed for each driver
177 in Section 3), for the austral spring (SON) and summer (DJF) seasons. This dataset will
178 hereafter be referred to as the observed FFDI.
179

180 *b) Forecasts of extreme fire weather using ACCESS-S1*
181

182 The Australian Community Climate and Earth System Simulator-Seasonal
183 forecast system version 1 (ACCESS-S1) is the Bureau of Meteorology's current
184 operational coupled model subseasonal to seasonal prediction system (Hudson et al.
185 2017). Based on the UK Met Office GC2 coupled model GloSea5 system (MacLachlan et
186 al. 2015), ACCESS-S1 uses the atmospheric Unified Model (UM; e.g. MacLachlan et al.
187 2015), the Nucleus for European Modelling of the Ocean (NEMO; e.g. Mogensen et al.
188 2009, 2012), the JULES land surface model (Best et al. 2011, Walters et al. 2017) and the
189 CICE sea ice model (Rae et al. 2015). ACCESS-S1 became operational at the Bureau of
190 Meteorology in August 2018, replacing the low resolution model POAMA (Alves et al.
191 2003; Hudson et al. 2011; Hudson et al. 2013).

192 The ACCESS-S1 system has a relatively high horizontal resolution of 25 km in
193 the ocean and roughly 60 km (N216) in the atmosphere. The stratosphere is well resolved
194 to above 1 hPa with 85 vertical levels in the atmosphere. Initial conditions for the
195 atmosphere are provided by interpolating zonal wind (u), meridional wind (v),
196 temperature, humidity and surface pressure from the European Centre for Medium-Range
197 Weather Forecasts (ECMWF)-Interim reanalysis (ERA-I; Dee et al. 2011) onto the
198 ACCESS-S1 atmospheric model grid. Initial conditions for sea-ice and the ocean are
199 provided from the NEMO variational assimilation produced at the UK Met Office (e.g.
200 Mogensen et al. 2009, 2012; MacLachlan et al., 2015). Soil moisture is initialised with
201 climatology (MacLachlan et al. 2015) and soil temperatures are interpolated from ERA-I
202 data.

203 The ACCESS-S1 system produces hindcasts comprising an 11-member ensemble.
204 Initial conditions are produced by a simple scheme that adds randomly sampled 7-day

differences from ERA-I (also rescaled to represent analysis uncertainty) into the atmospheric initial state (Hudson et al. 2017), and model uncertainty is provided by the stochastic backscatter scheme (MacLachlan et al. 2015). Hindcasts are initialised on the 1st, 9th, 17th and 25th of each month for the period 1990-2012, and we use daily- and weekly-mean output data for the first three weeks of each hindcast. We define a lead time of one week as the mean of the first week of each hindcast, a lead time of two weeks as the mean of the second week of each hindcast, and a lead time of three weeks as the mean of the third week of each hindcast. We aggregate the data into each season based on the validity/target date, as opposed to the start date, for each week. Hindcast anomalies are formed relative to the hindcast model climatology, which is a function of both start date and lead time, and thus a first-order linear correction for model mean bias is made in a similar fashion to that of Stockdale (1997).

The FFDI for ACCESS-S1 is calculated in a similar fashion to that described in Section 2a by combining daily model output of maximum temperature, rainfall, wind speed, and vapour pressure, calibrated to the daily AWAP analyses using a quantile-quantile matching method applied to daily data and downscaled from 60 km to 5 km horizontal resolution (Bureau of Meteorology, 2019d; de Burgh-Day et al. 2020). The calibration is done using leave-one-out cross validation (leaving out the year to be calibrated). Each start date and lead time are treated independently. For a given start date / lead time forecast, in addition to using all ensemble members (which would give 11x23 points), the data for five days before and after the target date are used (to give 11x23x11 points). This increase in sample size better captures the distribution of the data, especially at the extremes, and it is less affected by the relatively short hindcast period.

228

229 *c) Assessment of relationships to extreme fire weather*

230

231 Previous studies have used composite and correlation analyses for assessing
232 relationships to fire weather in Australia. A composite-based approach can be
233 advantageous in allowing the positive (high) and negative (low) phases of a climate driver
234 to be assessed separately. This is particularly meaningful where a climate driver (such as
235 ENSO) shows asymmetric impacts on Australian climate (e.g. Marshall et al. 2014b, Power
236 et al. 2006). This asymmetry is obscured by a correlation approach which includes all years
237 and thus combines low and high climate driver phases. We therefore use a composite-based
238 approach for diagnosing how key drivers of Australian climate variability can modulate
239 extreme weekly mean fire weather conditions from observations, and how well these
240 relationships are represented in ACCESS-S1 in weeks two and three of the forecasts. For
241 this we create the composite probability of occurrence of extreme FFDI with respect to
242 each climate driver (detailed in Section 3) and assess significance using a z-score test for
243 event probabilities (Spiegel 1961). The probability of occurrence of extreme weekly-mean
244 FFDI for each mode of variability is assumed to be significanctly different than the mean
245 probability when the absolute value of z is greater than 1.96 (two tailed distribution).

246 For the z-score test, we account for the possibility that the weekly-mean FFDI in our
247 composites may not be comprised of independent samples, *N*, for modes of variability with
248 long persistence timescales (such as the IOD and ENSO) by computing the effective
249 sample size, $N_{eff} (\cong N \frac{1-\rho}{1+\rho})$, using the lag-1 autocorrelation ρ of FFDI at each grid box.

(We note that for shorter timescale drivers such as the SAM, MJO and blocking, the weekly-mean data may be considered independent, e.g. Marshall et al. 2014b, Marshall et al. 2020.) We also account approximately for the non-independence of ACCESS-S1 ensemble forecast members at lead times of 2-3 weeks in a similar fashion, but by calculating the autocorrelation coefficient by correlating (as a function of hindcast start) each ensemble member with the ensemble mean of the remaining 10 ensemble members at each grid box. The correlation coefficients are then averaged over the 11 realisations, from which we calculate N_{eff}. This reduces the sample size by a factor of about four over much of the continent. We note here that sample sizes for the model remain notably larger than those for the observations, and thus probability composites for ACCESS-S1 often show a larger spatial coverage of significant ratios compared with those observed.

d) Verification for forecasts of extreme fire weather

We assess forecast skill for predicting extreme fire danger using the Symmetric Extremal Dependence Index (SEDI; Ferro and Stephenson 2011). The SEDI score is recognised for its ability to provide meaningful results when verifying extremes (e.g. North et al. 2013, Marshall et al. 2014b, White et al. 2014, Haiden and Duffy 2016, Singh et al. 2017, Marshall et al. 2020), where many other standard verification scores become degenerate in dealing with rare events and small sample sizes (Casati et al. 2008; Hogan and Mason, 2012; Ferro and Stephenson, 2011). Put another way, as rarity increases, many scores tend towards a meaningless limit, usually zero, irrespective of whether the forecast system is skilful or not. However, of the non-degenerate skill scores reviewed by Hogan

and Mason (2012), the SEDI score combines more desirable properties than any other, including equitability, difficulty to hedge and base-rate independence. Based on a 2×2 contingency table, the SEDI score is computed from the hit rate (H) and the false alarm rate (F) at each grid location, using equation (2):

$$SEDI = \frac{\log F - \log H - \log(1-F) + \log(1-H)}{\log F + \log H + \log(1-F) + \log(1-H)} \quad (2)$$

An FFDI forecast is a "hit" if it and the corresponding observation both exceed a chosen threshold – the 90th percentile in our study – and a "false alarm" if the forecast exceeds the threshold but the observed does not. SEDI scores greater than zero indicate skill better than for random forecasts, and scores less than zero indicate worse skill.

To calculate SEDI scores, we assume that the forecasts starting 8 days apart in each month (1st, 9th, 17th and 25th) are independent events, which is reasonable given that we are verifying subseasonal forecasts using weekly-averaged periods, and we construct the 2×2 contingency table using data from both weeks 2 and 3 of the forecast. The ensemble members are pooled, and each individual ensemble member adds to the counts in the contingency table before the SEDI score is calculated (Marshall et al. 2014b). We have found this to be more appropriate than (i) using the ensemble mean forecast for the contingency table (which leads to underestimation of event frequency) and (ii) calculating SEDI scores for each ensemble member and averaging the result (which leads to undefined SEDI scores where one or more entries in the contingency table equals zero.) The confidence interval of the SEDI is estimated using the formula for the standard error (S_{SEDI}; Ferro and Stephenson 2011), which is computed at each grid location from the hit rate,

false alarm rate, sample size n and base rate p (the relative frequency with which extreme fire danger is observed to occur),

$$s_{SEDI} = \frac{2\left|\frac{(1-H)(1-F)+HF}{(1-H)(1-F)}\log[F(1-H)] + \frac{2H}{1-H}\log[H(1-F)]\right|}{H\{\log[F(1-H)] + \log[H(1-F)]\}^2}\sqrt{\frac{H(1-H)}{pn}} \quad (3)$$

where $pn = a + c$ is the total number of observed events which we obtain from the contingency table (see Table 1 in Ferro and Stephenson 2011). We compute the 95% confidence intervals at each grid point as SEDI ± 2*S_{SEDI} (where S_{SEDI} estimates the standard deviation) and we consider SEDI scores to represent useful forecast skill (i.e. better than a random forecast) when confidence intervals comprise positive values only.

3 Climate driver impacts on extreme fire weather over Australia

a) Event probability thresholds

We define extreme fire danger based on weekly-mean FFDI values exceeding the 90th percentile, which is a commonly accepted threshold in assessing climate extremes on subseasonal to seasonal timescales including extreme temperature and rainfall (Alexander and Arblaster 2009, Perkins et al. 2012, Marshall et al. 2014b, White et al. 2014, Marshall et al. 2020). This inherently assumes the persistence of extreme fire weather over several consecutive days, rather than the occurrence of a single daily event. Figure 1 shows the 90th percentile threshold for weekly-mean FFDI from observations (left column), and from

ACCESS-S1 calibrated hindcasts for lead times of 2 and 3 weeks formed using individual ensemble members (right column), for SON (top row) and DJF (bottom row).

Observed FFDI threshold values above 50 (the level where human impacts of bushfire rapidly increase, e.g. Blanchi et al. 2010) typically occur over the subtropical inland regions of Australia where daytime temperatures are generally high and humidity is low, while thresholds are relatively low closer to the more temperate coastal regions. In particular, the lowest FFDI threshold values of less than 10 occur around the southwest and southeast Australian coasts, with orographic enhancement of low values (green shading) apparent along the Great Dividing Range in eastern Victoria and southern New South Wales. The large variation in threshold values across Australia in Figure 1 shows how extreme fire conditions do not pertain to a single FFDI value or category, but rather significant fire activity occurs across a range of values depending on the location of interest. This points to the appropriateness of a percentile-based fire danger rating system as a future alternative to the current system which categorises fire danger based on absolute values of the FFDI. (We also note the absence of vegetation types and state in the calculation of FFDI as another area for future improvement). Comparing the thresholds from ACCESS-S1 with those observed indicates remarkably good agreement both in spatial distribution and magnitude. We expect this agreement in magnitude because we are using calibrated data, while the spatial detail partly reflects the high model resolution and relatively good depiction of the relevant dynamics and circulation.

Based on exceedance of the 90th percentile thresholds displayed in Figure 1, we create the composite probability of occurrence of extreme FFDI with respect to the ENSO (Section 3b), IOD (Section 3c), SAM (Section 3d), MJO (Section 3e), and two modes of

337 persistent high pressure system in the Australian region (Section 3f). Detailed definitions
338 of each regime are provided in the subsections below. We consider covarying relationships
339 between climate drivers (e.g. the relationship of the IOD with ENSO; Meyers et al. 2007)
340 by using linear regression to remove residual driver signals from the analyses (e.g. Lim et
341 al. 2019). In doing so, we find little contamination by covarying drivers on the weekly
342 timescale (e.g. Marshall et al. 2014a). Probability composites are computed by counting
343 the number of instances at each grid location for which the weekly-mean FFDI value is
344 greater than the event threshold value as displayed in Figure 1, and then dividing by the
345 total number of samples in the composite. We display probability composites as ratios
346 relative to the mean decile probability of occurrence (nominally 0.1), so that probabilities
347 greater than one indicate an increased likelihood of an upper decile event, and probabilities
348 less than one indicate a decreased likelihood.
349

350 *b) Event probabilities associated with ENSO*

351

352 Several indices can be used to characterise ENSO, including the atmosphere-based
353 Southern Oscillation Index (SOI; formulated as the Darwin minus Tahiti anomalous sea
354 level pressure difference) and the ocean-based Niño-3, Niño-3.4, Niño-4 indices which
355 capture ENSO events with their strongest surface signal in the eastern Pacific Ocean.
356 ENSO events that have their strongest signal in the central Pacific are characterised using
357 the Modoki Index (Ashok et al. 2007). Here we use Niño-3.4, a popular index used for
358 measuring ENSO strength, which is formulated by averaging sea surface temperature
359 anomalies over the box domain 5°S-5°N and 170°-120°W. Previous work has found that

all ENSO indices accord well in their relationships to Australian rainfall variability (e.g. Risbey et al. 2009), although the sensitivity of the response can vary by location and season depending on the index used (e.g. Taschetto and England 2009), and thus future work should explore any differences in their relationships to fire weather variability and extremes. We construct the Niño-3.4 index for observations using sea surface temperature data from the global optimum interpolation analyses of Reynolds and Smith (1994), and we calculate the observed and hindcast indices as anomalies relative to their respective climatologies. We identify El Niño episodes when index anomalies are greater than one standard deviation above the mean, and La Niña episodes when index anomalies are less than one standard deviation below the mean.

Figure 2 shows a predominant increase in the observed likelihood of extreme fire weather over Australia in SON and DJF in association with El Niño. The increases are largest in SON over southeastern Australia where up to three times the normal likelihood of extreme fire conditions is observed. These results are complementary to previous studies that link El Niño to fire danger (e.g. Love and Downey 1986, Williams and Karoly 1999, Williams et al 2001, Verdon et al. 2004, Long 2006, Lucas et al. 2007) and fire activity (Felderhof and Gillieson 2006, Nicholls and Lucas 2007, Harris et al. 2008, Harris et al. 2014, Mariani et al. 2016) in Australia. The signal is weaker in DJF than in SON over many areas, particularly in South Australia where a decrease in extreme fire weather frequency occurs during El Niño. This is consistent with earlier studies (e.g. Dowdy 2018, Harris and Lucas 2019) where a weak and non-significant relationship to upper decile FFDI has been identified at the seasonal timescale using longer datasets. The El Niño relationship to fire weather occurs concomitant with reduced rainfall and enhanced daytime temperatures (e.g.

383 Nicholls et al. 1996, Meyers et al. 2007), although reduced relative humidity is shown to
384 be the FFDI parameter that is most strongly affected by ENSO (Williams and Karoly 1999).
385 The relationship to extreme fire weather is reversed during La Niña with broadscale
386 decreases observed over most of the continent (Figure 2), concomitant with enhanced
387 rainfall, reduced daytime temperatures and increased relative humidity (Nicholls et al.
388 1996, Williams and Karoly 1999, Meyers et al. 2007). These appear strongest in the north
389 and east during SON, and in the east and west during DJF, where the likelihood of extreme
390 fire conditions is less than half of the normal occurrence. Again, we see some areas that do
391 not follow this relationship, notably near the southwestern coast of western Australia where
392 increases of up to double the normal likelihood are observed in SON in association with
393 La Niña (also noted by Williams and Karoly 1999). These highlight asymmetries in the
394 extreme fire weather responses to El Niño and La Niña, possibly due to non-linearities in
395 the ENSO relationships to FFDI parameters including rainfall (e.g. Power et al. 2006, Cai
396 et al. 2010, King et al. 2013, Chung and Power 2017).
397 ACCESS-S1 neatly reproduces the observed relationships of ENSO to extreme fire
398 weather over Australia. This includes the peak increase in extreme fire weather likelihood
399 over southeastern Australia in SON during El Niño, the decrease over South Australia in
400 DJF during El Niño, and the increase over southwestern Western Australia in SON during
401 La Niña. There are some areas where the model fails to adequately reproduce the observed
402 relationships however, particularly when observed probabilities of extreme fire conditions
403 are high. These include (i) over parts of the northwestern Australia in SON, (ii) along parts
404 of the southern coastline including in Tasmania in DJF, and (iii) along a coastal strip
405 straddling the Queensland / New South Wales border during El Niño in SON. In spite of

406 these examples of where the ENSO teleconnection is underdone, our results show that
407 ACCESS-S1 generally depicts well the Australian circulation response to ENSO during
408 the first 2-3 weeks of the hindcast.
409

410 *c) Event probabilities associated with the IOD*
411

412 Variability in the IOD is commonly measured using the dipole mode index (DMI; Saji
413 et al. 1999), formulated as the difference in SST anomaly averaged over a box domain in
414 the tropical western Indian Ocean (10°S-10°N and 50°-70°E) and the tropical southeastern
415 Indian Ocean (10°S-equator and 90°-110°E). We construct the DMI for observations using
416 sea surface temperature data from the global optimum interpolation analyses of Reynolds
417 and Smith (1994), and we calculate the observed and hindcast indices as anomalies relative
418 to their respective climatologies. The high index (or positive phase) of the IOD occurs
419 when index anomalies are greater than one standard deviation above the mean, and the low
420 index (or negative phase) occurs when index anomalies are more than one standard
421 deviation below the mean. We perform our analysis for SON only, due to the seasonal
422 phase locking of the IOD from about June to December with its peak activity in austral
423 spring (Saji et al. 1999).
424 Figure 3 shows an increase in the observed frequency of extreme fire weather during
425 the positive IOD phase, and a decrease during the negative IOD phase, over much of
426 Australia. These relationships appear strongest across tropical northern Australia and in the
427 southeast, where the observed frequency of occurrence is doubled when the IOD is positive
428 and halved when the IOD is negative, compared to normal. By contrast, the relationships

appear weakest in Western Australia for the positive IOD phase, and in parts of central Australia. Similar results were found by Harris and Lucas (2019) for upper decile FFDI at the seasonal timescale. The IOD relationship to extreme fire weather occurs concomitant with a predominant decrease in Australian rainfall during the positive IOD and increase in Australian rainfall during the negative IOD (e.g. Meyers et al. 2007, Risbey et al. 2009).

ACCESS-S1 reproduces the observed relationships of the IOD to extreme fire weather over Australia but with a clear underestimation of the high probability ratios during the positive IOD phase. The observed relationship for the negative IOD phase is, however, captured by the model reasonably well. As such, a non-linearity is apparent in the model's response to the IOD over much of southern Australia where the IOD shows its strongest relationship to rainfall (Meyers et al. 2007, Risbey et al. 2009). We therefore suggest that this model shortcoming may be related to rainfall and SST biases across the Indian Ocean in ACCESS-S1 (a wet bias over the central-western Indian Ocean and a dry bias over the eastern Indian Ocean), both of which are prominent in SON, develop rapidly and intensify with lead time (Zhou et al. 2015; Lim et al. 2016). It is likely that these biases negatively impact the teleconnection between the Indian Ocean and Australian climate (Lim et al. 2016).

d) Event probabilities associated with the SAM

We represent the SAM using an index that captures the variability of mean sea level pressure (MSLP) due to the SAM (e.g. Marshall et al. 2012, Marshall et al. 2014b). Weekly SAM indices are obtained from the principal component time series of the leading

empirical orthogonal function (EOF) of weekly-mean zonal-mean MSLP computed between 25°S and 75°S, which we compute separately for observations using NNR1 data and for the ACCESS-S1 hindcasts. Before computing the EOFs, the seasonal cycle is removed and grid points are weighted by the square root of the cosine of latitude (to compensate for the geographical decrease in grid size towards the pole). The EOF analysis is conducted on the base period 1990 to 2012 and each EOF is based on the covariance matrix. For ACCESS-S1 we calculate EOFs using each ensemble member for each lead time. The weekly observed and modelled SAM indices are normalised by their respective standard deviations. The high index (or positive phase) of the SAM occurs when the pressure anomaly is low on the pole and the midlatitude westerly jet is shifted poleward, with index values exceeding one standard deviation above the mean. The low index (or negative phase) occurs when the pressure anomaly is high on the pole and the midlatitude westerly jet is shifted equatorward, with index values of more than one standard deviation below the mean.

An increase in the observed likelihood of extreme fire weather occurs over much of Australia during the negative SAM phase in SON and DJF (Figure 4), concomitant with enhanced temperatures and reduced rainfall, particularly over the east and south-east (Hendon et al. 2007, Marshall et al. 2012, Min et al. 2013, Marshall et al. 2014b). These increases are generally largest in SON, with more than double the normal likelihood of extreme fire conditions observed over eastern and southern Australia including near the border of Western Australia and South Australia, parts of eastern Queensland and Victoria, and most of New South Wales. These results are consistent with Harris and Lucas (2019) and Lim et al. (2019), who show the negative SAM to be a key influence for elevated fire

475 weather across much of the country, particularly in Queensland and NSW, during austral
476 spring. In DJF, the likelihood of extreme fire conditions occurring is up to double the
477 normal likelihood over much of the east, south and the tropical north. Notable exceptions
478 are the southwestern coastal strip south of the Ningaloo Reef in SON and much of Victoria
479 in DJF. Conversely, the positive phase of the SAM acts to decrease the observed
480 probabilities over much of Australia in both seasons, particularly for the eastern two thirds
481 of the country in SON and in the southeast in DJF where the likelihood of extreme fire
482 conditions is less than half of the normal occurrence. This is consistent with the impact of
483 the positive SAM to enhance rainfall and reduce the daytime warming, related to enhanced
484 cloud cover and reduced insolation (e.g. Jones 1991, Nicholls et al. 1997, Power et al. 1998,
485 Jones and Trewin 2000) in addition to adiabatic cooling through induced upward motion
486 in the subtropics (Hendon et al. 2013, Lim et al. 2013). We note the approximate symmetry
487 between the positive and negative SAM impacts on extreme fire conditions, seen most
488 clearly in SON.

489 ACCESS-S1 reproduces the observed relationships to extreme fire weather over much
490 of Australia, although the strength of the teleconnections is generally weaker than
491 observed. ACCESS-S1 emphasises the relationships over eastern Australia where they
492 appear strongest in observations. There is room for improvement in the depiction over
493 southern Australia for the negative SAM phase in DJF, which may reflect biases in the
494 model's depiction of SAM circulation anomalies to the south of Australia during the first
495 2-3 weeks of the hindcast under the influence of its drifting basic state (Marshall et al.
496 2012, Marshall et al 2014b, Lim et al. 2016).
497

e) Event probabilities associated with the MJO

The state of the MJO is depicted using the Real-time Multivariate MJO (RMM) indices from Wheeler and Hendon (2004). The two RMM indices, RMM1 and RMM2, capture the eastward-propagating large-scale structure of the MJO in zonal wind and convection along the equator to provide a measure of the strength and phase of the MJO. We form the observed RMM index by projecting daily anomaly data onto the leading pair of EOFs of the combined standardised fields of equatorially-averaged (15°N-15°S) outgoing longwave radiation (OLR), 850 hPa zonal wind, and 200 hPa zonal wind from NNR1. This leading pair of EOFs are derived from data that are not subject to any band pass filtering and so can be used to assess both real time evolution of the MJO and its prediction with forecast data.

For ACCESS-S1 we create predicted RMM1 and RMM2 indices by projecting the model's predicted anomalies of equatorially averaged outgoing longwave radiation and zonal winds at 200 and 850 hPa onto the observed EOF pair, as described by Rashid et al. (2011). Prior to projecting the daily observed and predicted anomalies onto the observed EOF pair, interannual variability is removed by subtracting the previous 120-day mean. For the ACCESS-S1 hindcasts this involves subtracting a 120-day mean that is created for lead time *n* days as the mean of the previous 120-*n* days of observations up to the start of the forecast plus the *n* days of the forecast. RMM1 and RMM2 may equivalently be expressed as a daily amplitude ($= \sqrt{RMM1^2 + RMM2^2}$) and phase ($= \tan^{-1}(RMM2 / RMM1)$), which is useful for the construction of MJO composites. We

use the same eight phases as defined by Wheeler and Hendon (2004), with the MJO deemed to be in an active cycle when the RMM index amplitude is greater than one.

Figures 5-8 show the probability composite maps for each active MJO phase. An increase in the observed frequency of extreme fire weather during SON occurs across much of northern and eastern Australia in MJO phase 1 (Figure 5), southern Australia in phases 2 and 3 (Figure 5), and much of the country in phases 7 and 8 (Figure 6). The largest increase occurs in phase 3 when a tripling of the likelihood of extreme fire weather occurs concurrent with a strong increase in the likelihood of extreme heat (Marshall et al. 2014b) and a decrease in the likelihood of above average (Wheeler et al. 2009) and extreme rain (Marshall et al. 2020). At this time, when the convective phase of the MJO is active over the Indian Ocean, the probability of weekly-mean rainfall is low in conjunction with a strong anticyclonic anomaly in the midlevel circulation and subsidence over southern Australia (Wheeler et al. 2009). Conversely, an observed decrease in extreme fire weather frequency across most of Australia in MJO phase 5 and eastern Australia in phase 6 (Figure 6) occurs concurrently with enhanced rainfall probabilities and low geopotential height anomalies (Wheeler et al. 2009).

The likelihood of extreme fire weather in DJF is also observed to change in various MJO phases throughout Australia, reflecting the importance of both the local and remote impacts of the MJO (e.g. Wheeler et al. 2009). An increase in the frequency of extreme fire weather over northern Australia in phases 8, 1 and 2 occurs as a direct response to the suppressed convective phases of the MJO (when the MJO is active in the western hemisphere), while a substantial reduction during phases 4, 5 and 6 occurs as a direct response to the active convective phases of the MJO. This again follows the MJO

543 relationships to extreme heat (Marshall et al. 2014b) and extreme rain (Marshall et al. 2020).
544 The opposite signal to that over the north can be seen across southern Australia in many
545 phases – in particular, high probability ratios in phases 5 and 6 and low probability ratios
546 in phases 8 and 1. This occurs coincident with warm northerly and cool southerly low-level
547 wind anomalies respectively over southern Australia (Wheeler et al. 2009). High
548 probability ratios occur over much of eastern Australia in phases 6-7 (from southern
549 Queensland to Tasmania) and phase 8-1 (Queensland and New South Wales).
550 ACCESS-S1 is often able to capture both the tropical and extratropical signals. Given
551 the ability of ACCESS-S1 to predict the MJO to lead times of 25 days in DJF and 30 days
552 in SON (Marshall et al. 2020), this gives promise for predicting extreme fire weather events
553 2-3 weeks ahead when teleconnection to the MJO is strong. Yet there is notable room for
554 improvement in some MJO phases when the model does not adequately capture the remote
555 signal observed over parts of southern Australia – for example phases 4 and 6 in SON and
556 phases 5-7 in DJF. There is also an underestimation of the peak magnitude for phase 3 in
557 SON when the MJO shows its strongest observed relationship to extreme fire weather.
558 These highlight examples where improved representation of the MSLP/circulation
559 response to the MJO is needed (e.g. Wang and Hendon 2020).
560

561 *f) Event probabilities associated with persistent anticyclones in the Australian region*

562 *3.f.1 Split-flow blocking*

563

564 Persistent anticyclones are recognised as having important influences on Australia's
565 agricultural districts and water catchments. Marshall et al. (2014b) show there are two

566 distinct modes of persistent anticyclone that have contrasting impacts on subseasonal
567 climate variability and extremes over Australia. The mode that blocks and separates the
568 midlatitude westerly airstream into two branches, defined as 'split-flow blocking', is
569 represented by a simple index that describes the degree of splitting of 500 hPa zonal winds
570 over the Australian continent (Pook and Gibson 1999). This splitting occurs at latitudes
571 that are well poleward of the sub-tropical ridge (Equation 4).
572
573 $$\text{blocking} = 0.5(U_{25} + U_{30} - U_{40} - 2U_{45} - U_{50} + U_{55} + U_{60}) \quad (4)$$
574
575 where U_y represents the total 500 hPa zonal wind at latitude y°S. A high split-flow blocking
576 index describes enhanced 500 hPa westerly flow at high and low latitudes with reduced
577 flow at mid-latitudes, whereas a low index describes the opposite situation with enhanced
578 flow at mid-latitudes. Periods of split-flow blocking typically result in a reduction in
579 orographically-derived rainfall in western Tasmania, and increased rainfall in eastern
580 Tasmania, due to the anomalous absence of westerly and south-westerly wind streams
581 (Pook and Gibson 1999). As this occurs, a smaller cyclonic component forms on the
582 equatorward side of the blocking high which breaks away to create a cutoff low pressure
583 system (Coughlan 1983) and brings significant rainfall to southeast mainland Australian
584 (Pook et al. 2006).
585 Here we evaluate impacts of split-flow blocking at 140°E, which is regarded as a
586 typical longitude for blocking in the Australian region to influence rainfall over much of
587 Australia and over the southeast in particular (e.g. Pook et al. 2006, Risbey et al. 2009).
588 We construct the split-flow blocking index for observations using weekly-mean 500 hPa

589 zonal wind data from NNR1, and we calculate the observed and hindcast indices as
590 anomalies relative to their respective climatologies. Episodes of high blocking activity are
591 identified when index anomalies are greater than one standard deviation above the mean,
592 and low blocking activity when index anomalies are less than one standard deviation below
593 the mean (e.g. Marshall et al. 2014a).

594 Figure 9 shows an increase in the observed frequency of extreme fire weather over
595 southern Australia when blocking activity is low (when the mid-latitude westerly flow is
596 enhanced), and a decrease over southern Australia when blocking activity is high (when
597 the mid-latitude westerly flow is reduced), corresponding to the local rainfall and 500 hPa
598 geopotential height responses to blocking at midlatitudes (Marshall et al. 2014a).
599 Probabilities maximise over southeastern Australia during episodes of low blocking, where
600 extreme fire conditions are up to two and a half times more likely than normal in both
601 seasons. The teleconnection to northern Australia shows a mixed signal that varies by
602 season. The relationship is reversed in the far north (more so in DJF during the northern
603 wet season) and in parts of southern Queensland where an increase in extreme fire weather
604 frequency occurs during episodes of high split-flow blocking. ACCESS-S1 broadly
605 reproduces the observed spatial patterns reasonably well, although again there is a general
606 underestimation of the peak magnitudes, and the model is unable to capture the relationship
607 to low blocking in DJF over the southeast. This is an area for further investigation as it may
608 suggest a model issue in representing the strong seasonal cycle of split-flow blocking in
609 the Australian region, which shows a minimum frequency of occurrence in austral summer
610 (Pook et al 2013, Marshall et al. 2014a).

611

612 *3.f.2 Subtropical Ridge Tasman Highs*

613

614 A second mode of persistent anticyclone was differentiated from the split-flow
615 blocking mode by Marshall et al. (2014b) when they discovered that the relationship of
616 each regime to Australian heatwaves was distinctly different. When high pressure systems
617 persist over the Tasman Sea in the vicinity of the subtropical ridge, about 10° north of the
618 split-flow blocking region, they provide northerly anomalous flow to southeastern
619 Australia, increasing the likelihood of an extreme heat event over much of southern
620 Australia and reducing the likelihood over much of northern Australia. Importantly, the
621 500 hPa westerly airstream does not split over the Australian continent as is the case for
622 split-flow blocks. Marshall et al. (2014b) devised a simple index for these events, dubbed
623 the Subtropical Ridge Tasman High (STRH) index, using weekly-mean MSLP data
624 averaged over the box region defined by 150°E-165°E and y°S±7.5°, where y°S is the
625 climatological central latitude of the subtropical ridge determined for each month (ranging
626 from 27.5°S in August to 40°S in February). We construct the STRH index for observations
627 using NNR1 data and again calculate the observed and hindcast indices as anomalies
628 relative to their respective climatologies. Episodes of high STRH activity are identified
629 when index anomalies are greater than one standard deviation above the mean, and low
630 STRH activity when index anomalies are less than one standard deviation below the mean
631 (e.g. Marshall et al. 2014b).

632 Figure 10 shows an increase in the observed frequency of extreme fire weather over
633 the southern Australian temperate zone (south of about 30°S) and around some coastal
634 regions to the north when STRH activity is pronounced in SON and DJF. Further inspection

635 (of extreme temperature and rainfall probabilities; not shown) suggests that the southern
636 Australian signal results from the northerly advection of warm subtropical air into the south
637 (Marshall et al. 2014b) where the likelihood of drier conditions is also increased.
638 Subsequently, the flow of heat away from the subtropics (with increased onshore flow) is
639 reflected in the reduced likelihood of extreme fire weather observed there, most
640 pronounced over southern Queensland and northern New South Wales in the proximity of
641 the Tasman Sea (Figure 10). The enhanced signal over the northern coastal regions,
642 particularly during the DJF north Australian wet season, may suggest anomalous drying
643 via transport of moist tropical air away from these regions, thus increasing the likelihood
644 of elevated fire weather conditions occurring.

645 During episodes of low STRH activity (i.e. anomalous low pressure over the
646 Tasman Sea), the opposite picture emerges in SON with an increase in the observed
647 frequency of extreme fire weather in the Australian subtropics, maximised over southern
648 Queensland, and a decrease at temperature latitudes further south (Figure 10). This signal
649 is confined to the east in DJF and a reduction in extreme fire weather frequency is seen
650 elsewhere across the country. This pattern largely reflects the STRH relationship to
651 extreme heat during DJF (Marshall et al. 2014b), influenced by the development of the
652 monsoon trough over central and northern Australia (e.g. Hendon and Liebmann 1990).

653 ACCESS-S1 captures the observed relationship to extreme fire weather in some
654 areas but not in others. Observed relationships are generally better simulated over the
655 southern and eastern regions than they are over north and west, again highlighting
656 challenges in capturing remote teleconnections. However, for eastern Australia, the model
657 underestimates the peak magnitudes and is unable to capture the observed relationship to

low STRH activity in DJF. This likely points to biases in the model's representation of negative MSLP anomalies found to the southeast of Australia during the first 2-3 weeks of the hindcast under the influence of its drifting basic state, which may also be a source of error in the depiction of extreme fire weather over southern Australia for the negative SAM phase in DJF (Section 3d).

4 Prediction of extreme fire weather over Australia

a) Overall prediction

The ability of ACCESS-S1 to predict extreme fire weather in association with each climate driver is related to the model's ability to (i) predict the climate driver and (ii) simulate the relationship between the climate driver and extreme fire weather over Australia. Given that ACCESS-S1 provides skilful prediction of the climate drivers assessed here on timescales from weeks to seasons ahead, based on the correlation and root mean square error statistics in Hudson et al. (2017), we now turn our attention to the ability of the model to predict extreme fire weather events in association with each climate driver at lead times of 2-3 weeks. Using the SEDI metric described in Section 2c, we begin by scoring weekly-mean forecasts for weeks 2 and 3 combined, using all available forecasts for SON and DJF, to examine the spatial distributions of skill for predicting extreme fire weather irrespective of any particular climate driver (i.e. the average climate driver activity is weak/neutral across all forecasts). Pleasingly, Figure 11 shows that the SEDI is positive almost everywhere over the continent, with the largest values seen over central,

681 southwestern and southeastern regions in SON, and over northern and eastern regions in
682 DJF. These skill maps will form the basis for assessing the role of each climate driver in
683 the prediction of extreme fire weather for the remainder of this paper. Specifically, we
684 compute the difference in SEDI for hindcasts stratified by the phase of a given climate
685 driver, relative to when the climate driver is weak, at the verification time to gain insight
686 into how and when each driver modulates predictive skill; this occurs where SEDI
687 differences are significantly greater than zero in the analyses that follow (Figures 12-18).
688

689 *b) Event prediction associated with ENSO*

690

691 ACCESS-S1 shows improvements in SEDI skill for predicting extreme fire weather
692 over parts of eastern and northern Australia in SON during episodes of El Niño, compared
693 to when ENSO is neutral (Figure 12). These regions coincide with where the odds of
694 extreme fire weather are elevated during El Niño (Figure 2), highlighting a window of
695 forecast opportunity when reduced rainfall over Australia occurs in conjunction with an
696 increase in broad-scale surface pressure (e.g. Risbey et al. 2009). There is little role for El
697 Niño in improving the prediction of fire weather extremes over southwestern and central
698 Australia, nor in a coastal strip straddling the Queensland / New South Wales border where
699 the model does not capture the observed increase in extreme fire weather frequency during
700 El Niño (ref. Figure 2). Impressively during La Niña however, an improvement in skill
701 occurs near the southwest West Australian coast (Figure 12) where the probability of
702 extreme fire weather occurring is elevated in SON (Figure 2). Improvements in skill during
703 El Niño and La Niña also occur over broad areas in DJF, most notably in central northern

Australia during El Niño when probabilities of occurrence are high. These results highlight an important role for ENSO in providing predictive skill over many regions likely to experience extreme weather conditions during the September-March Southern Australian bushfire season.

c) Event prediction associated with the IOD

The IOD provides improved skill for predicting extreme fire conditions in SON over much of Australia during its high and low phases (Figure 13). This includes large parts of eastern Australia where the observed frequency of extreme fire weather is elevated during the positive IOD phase (Figure 3), thus indicating usefulness in the forecasts at these times. We note that the role of the positive IOD for improving forecast skill is reduced over part of southeast Queensland and northeast New South Wales. For Tasmania, improved skill is achieved over the east and north of the state where the model captures the observed signal during the positive IOD. When the IOD is negative, forecast skill is improved over a larger area of Australia compared to when the IOD is positive, which likely reflects the model's better overall depiction of the IOD relationship to extreme fire weather during the negative phase. We therefore suggest that further improvements to the skill for predicting extreme fire weather related to the IOD may be achieved by improving the SST and rainfall biases over the Indian Ocean in ACCESS-S1 (Lim et al. 2016).

d) Event prediction associated with the SAM

In SON, improvements in prediction skill occur over large parts of eastern and northern Australia during both the high and low SAM phases, in southwest Western Australia during the high SAM phase, and near the central-south coast during the low SAM phase (Figure 14). Importantly, this includes key regions in the southern half of the country where the odds of extreme fire weather are elevated when the SAM is in its negative phase (concurrent with higher temperatures, reduced rainfall and enhanced westerlies) (Figure 4). Notably, there is room for model improvement over parts of eastern Queensland during the low SAM phase when there is no clear role for the SAM in improving the prediction of fire weather extremes. During DJF, the largest skill improvements occur in the southeast in association with the SAM, including areas where likelihood of extreme fire conditions is nearly twice the normal occurrence (Figure 4). These improvements extend up the east coast of Queensland and along the Australian northwest coast during the low SAM phase, and thus the SAM also provides skill for predicting extreme fire conditions over these regions.

e) Event prediction associated with the MJO

The role of the MJO in improving the prediction of extreme fire weather varies regionally by MJO phase and season. In SON (Figure 15), notable improvements in skill include over eastern Australia in phase 1, southern Australia in phases 2, 3 and 4, and southwestern Australia in phases 6 and 7, where the chances of extreme fire weather are

748 elevated when the MJO is strong in these phases (Figures 5 and 6). Improvements in skill
749 are also seen over parts of eastern Australia in phases 4, 5 and 6 when the MJO acts to
750 decrease the chances. During DJF (Figure 16), improvements in skill for predicting
751 extreme fire weather due to the MJO are seen in eastern Australia in phase 1 and northern
752 Australia in phases 1, 2 and 3 when the MJO acts to increase the chances of extreme fire
753 weather in both the observations and the model (Figures 7 and 8). Improvements in skill
754 also occur in phases 4-7 over parts of southern Australia where the MJO acts to increase
755 the frequency of extreme fire weather in observations, but where the model underperforms
756 in its representation of the frequency of those extremes in relation to the MJO (Section 3e).
757 Windows of forecast opportunity are therefore seen across a range of MJO phases and
758 geographical regions in each season; most impressively over southern Australia in phase 3
759 during SON, and over northeastern Australia in phase 1 during DJF, when the MJO shows
760 its strongest seasonal relationships to extreme fire weather in association with anomalous
761 dry and warm conditions (e.g. Wheeler et al. 2009, Marshall et al. 2014b, Marshall et al.
762 2020).
763

764 *f) Event prediction associated with persistent anticyclones in the Australian region*

765 *4.f.1 Split-flow blocking*

766

767 Figure 17 shows more widespread improvements in prediction skill when split-flow
768 blocking activity is low, compared to when activity is high, in SON and DJF. Notably,
769 these improvements coincide with the increases in extreme fire weather frequency over
770 much of eastern Australia during episodes of low blocking (Figure 9). Prediction skill is

771 also improved over northwestern Australia in DJF where the likelihood of extreme fire
772 weather is reduced during low blocking activity. During episodes of high split-flow
773 blocking activity in SON, we see notable improvements in prediction skill near the Gulf of
774 Carpentaria and over parts of southern Queensland where the odds of extreme fire weather
775 are elevated, despite the model's underestimation of the observed magnitudes (Figure 9).
776 Overall, ACCESS-S1 appears to perform most favourably in SON over the Australian
777 extratropics where the impacts of low split-flow blocking on fire weather extremes are
778 most pronounced.
779

780 *4.f.2 Subtropical Ridge Tasman Highs*
781

782 In SON, improvements in prediction skill occur over large parts of eastern and
783 northern Australia during episodes of both high and low STRH activity (Figure 18).
784 Although somewhat patchy, these areas generally correspond to where the observed
785 likelihood of extreme fire weather is reduced during high STRH activity and enhanced
786 during low STRH activity (Figure 10). In DJF, improvements in skill correspond to where
787 the observed likelihood of extreme fire weather is enhanced over parts of coastal northern
788 Queensland and Victoria during high STRH activity, and parts of southern Queensland /
789 northern New South Wales during low STRH activity. Elsewhere the improvements in skill
790 generally coincide with reduced odds of extreme fire weather, during episodes of both high
791 and low STRH activity in DJF. We note that there is little improvement in skill in either
792 season near the southern coasts of Western Australia and South Australia, where the model

falls short in capturing the observed increases in extreme fire weather frequency during episodes of high STRH activity (Figure 10).

In summary, when considering persistent anticyclones in the Australian region as a source of subseasonal predictability for extreme fire weather in ACCESS-S1, the greatest benefits are generally seen over parts southern Australia in association with low split-flow blocking activity, and eastern Australia in association with low STRH activity, where their impacts on fire weather extremes are most pronounced.

5 Summary and conclusions

This study provides a comprehensive assessment of the role of key modes of subseasonal climate variability on extreme fire weather in Australia, and their depiction and prediction in the Bureau of Meteorology's ACCESS-S1 seasonal prediction system, during the austral spring (SON) and summer (DJF) Australian bushfire season. These modes of variability, or climate drivers, include the ENSO, IOD, SAM, MJO, and persistent high-pressure systems in the Australian region. (We assess the role of the IOD in SON only, due to its rapid demise from December.) We represent their relationships to extreme fire weather on the subseasonal timescale using the upper decile of weekly-mean FFDI for observations and for ACCESS-S1 hindcasts in weeks two and three. All climate drivers assessed here act to modulate the occurrence of extreme fire weather throughout Australia, and thus each driver is a potential source of multiweek predictability. The influence of each climate driver varies by location and season.

In SON, the observed likelihood of extreme fire weather increases over most of Australia in association with El Niño, the positive IOD, negative SAM, and low split-flow blocking. The prevalent climate conditions associated with these driver phases, and favourable to extreme fire conditions, include increased temperatures, reduced rainfall, enhanced wind speeds and lower relative humidity (Williams and Karoly 1999, Meyers et al. 2007, Risbey et al. 2009, Marshall et al. 2014a). The increases in extreme fire weather frequency are generally largest over the southeast where two to three times the normal likelihood is observed in association with these drivers. The role of the STRH is similar to that of split-flow blocking over subtropical latitudes (north of about 30°S) where an increase in extreme fire weather frequency occurs when STRH activity is low. When STRH activity is pronounced however, the southern Australian temperate regions experience warm airflow from the north (Marshall et al. 2014b) and the likelihood of extreme fire weather increases. One must therefore exercise caution when identifying persistent anticyclones in the Australian region as they can have very different impacts on extreme fire weather conditions for a given location, depending on their dynamical characteristics and location. The role of the MJO also varies by phase, with the largest observed impact during SON occurring in MJO phase 3 when a tripling of the likelihood of extreme fire weather occurs concurrent with hotter and drier conditions (Marshall et al. 2014b, Marshall et al. 2020).

In DJF, the driver relationships to extreme fire weather are broadly similar to those in SON, but with some notable exceptions. The peak increases are often observed to be weaker in DJF, especially over the southeast during El Niño, the negative SAM phase and MJO phase 3, and over eastern Australia when STRH activity is low. ACCESS-S1

simulates the observed modulation of extreme weekly-mean fire weather by each climate driver reasonably well in SON and DJF. However, the variation of the model's extreme fire weather event probabilities is often weaker than those observed in association with the SAM, MJO and persistent highs. There are also some instances where the model misses some of the observed high probability ratios, such as during the positive IOD phase in SON (possibly related to rainfall and SST biases across the Indian Ocean) and during the negative SAM phase in DJF (possibly due to biases in the model's depiction of SAM circulation anomalies). These highlight examples where the model's drifting mean state can adversely affect the driver teleconnections to Australia in the first few weeks of the hindcast.

To gain an indication of the relative influences of each climate driver on extreme fire weather at each location and in each season, we compare the drivers according to the magnitude of their probability ratios following the method of Risbey et al. (2009). In Figure 19 we show only the driver with the highest probability ratio at each grid point. This may be considered a crude estimate of their relative influences, keeping in mind that two or more drivers may have a similar influence at a particular grid point, but only the driver with the highest probability ratio will be shown. We also realise that the interplay between climate drivers can complicate the picture (e.g. Meyers et al. 2007, Risbey et al. 2009). Thus, the figure is intended to provide a qualitative overview of where and when each driver is most influential. We conduct the analysis for both observations and the model, to also gauge the relative influence of each climate driver as depicted by ACCESS-S1. Specifically, we are interested to see how the underestimated strength of the driver teleconnections in the model (discussed above) may impact their relative influences on extreme fire weather, compared to observations.

Figure 19 shows the MJO to be the leading observed driver of extreme fire weather in SON, in terms overall spatial coverage. As deduced from Figures 5 and 6, this primarily comes from the strong teleconnection in phase 3 over southern Australia including Tasmania, and from the suppressed convective phases 7, 8 and 1 over northern Australia. ENSO (El Niño) tends to dominate over the southeast mainland, central north and parts of the west coast, while the STRH (low phase) dominates over the central east. The IOD (positive phase), SAM (low phase) and blocking (low phase) each dominate extreme fire weather frequency in different parts of the country, although their footprints are relatively small and thus their signals appear largely masked by the other drivers. By comparison, the leading driver of extreme fire weather in ACCESS-S1 during SON is clearly ENSO (El Niño), in terms its widespread coverage across much of Australia. This highlights the model's weaker than observed representation of probability ratios in association with the other climate drivers. There appears to be better general agreement between observations and ACCESS-S1 for the DJF analysis, although the model's weaker than observed signals are evident in blocking (low phase) over the southeast, the SAM (low phase) over the southwest, and the STRH (low phase) over the central east where these drivers dominate in the observations (Figure 19).

In this study we use the SEDI deterministic skill score for binary events to assess prediction skill for forecasting extreme weekly-mean fire weather in association with each climate driver out to 2-3 weeks lead time. Each driver plays an important role in providing predictive skill for regions where ACCESS-S1 captures the high likelihood of experiencing extreme fire weather conditions during the spring and summer seasons, highlighting windows of forecast opportunity at lead times of 2-3 weeks that can be useful to regional

884 users. For SON, this constitutes parts of the north (El Niño, low STRH), east (El Niño,
885 MJO phase 1, low STRH), and south (negative SAM, MJO phases 2-4, low blocking)
886 including the southwest (La Niña, MJO phases 6-7) and southeast (positive IOD). For DJF,
887 this constitutes parts of the north (El Niño, MJO phases 1-3, negative SAM) and east (MJO
888 phase 1, low blocking, low STRH), including the northeast (high STRH) and southeast (El
889 Niño, negative SAM, high STRH). We note, however, that there are instances where SEDI
890 skill is reduced across some regions during active climate driver phases (Section 4), partly
891 related to model biases and systematic errors in the depiction of climate driver
892 teleconnections to Australia (Hudson et al. 2017, Marshall et al. 2020). As such, these areas
893 of reduced skill often occur where the model is unable to capture the observed relationships
894 to extreme fire weather, including over parts of the central east during the positive IOD
895 (SON) and far south during high STRH activity (both SON and DJF). Thus, we see scope
896 for improvement for ACCESS-S in its ongoing development with the Bureau of
897 Meteorology partner the UK Met Office (e.g. Walters et al. 2017).

898 The next version of the prediction system, ACCESS-S2, is soon to be released.
899 Improvements over ACCESS-S1, outlined in Hudson et al. (2017), include a larger
900 hindcast ensemble and improved initialisation. Future extensions of our work will explore
901 the depiction and prediction of climate driver impacts on fire weather variability and
902 extremes in ACCESS-S2, using the upcoming new Australian Fire Danger Rating System
903 (AFDRS) (Matthews et al. 2018). This work could include an investigation of relationships
904 with variables that the FFDI does not use, such as vegetation state. It could also include an
905 assessment of ENSO, IOD, and SAM related impacts on the seasonal timescale,
906 particularly important for austral spring when extended prediction of the SAM is possible

through its connection with ENSO and with variability in the Southern Hemisphere stratospheric polar vortex (Lim et al. 2019). Longer timescale impacts on extreme fire weather over Australia from projected trends in the SAM (e.g. Christensen et al. 2013) and split-flow blocking (Grose et al., 2012) are also of interest for future investigation.

Acknowledgements

This work is a collaboration between Research, Climate Services and Earth System Modelling at the Australian Bureau of Meteorology. The work was undertaken with the assistance of resources from the National Computational Infrastructure (NCI), which is supported by the Australian Government. We extend our thanks to Robin Wedd and Griffith Young for their work on the production and management of the ACCESS-S1 hindcasts, and to Harvey Ye, Andrew Dowdy and Chris Lucas for their work on the calculation of FFDI data at the Bureau of Meteorology. We are also grateful to Paul Fox-Hughes and Debra Hudson for generously giving their time to help improve the overall quality of this paper.

Declarations

Funding: The work was undertaken with the assistance of resources from the National Computational Infrastructure (NCI), which is supported by the Australian Government.

Conflicts of interest / Competing interests: The authors have no conflicts of interest to declare that are relevant to the content of this article.

Availability of data and material: Support for the AWAP gridded data, available in Jones et al. (2009), is provided by CSIRO and the Bureau of Meteorology. The AWAP data used in this paper are openly accessible from https://doi.org/10.4227/166/5a8647d1c23e0, under the CC BY-NC 4.0 International Licence. Support for the NNR1 gridded data, available in Kalnay et al. (1996), is provided by the NOAA/OAR/ESRL Physical Sciences Laboratory, Boulder, Colorado, USA. The NNR1 data used in this paper are openly accessible from https://psl.noaa.gov.

937 **References**

938

939 AFAC (2019) AFAC Independent Operational Review: A review of the management of
940 the Tasmanian fires of December 2018 – March 2019. Australasian Fire and Emergency
941 Service Authorities Council (AFAC), 64 pp,
942 http://www.fire.tas.gov.au/userfiles/AFAC/AFAC_Review.pdf

943

944 Alexander LV, Arblaster JM (2009) Assessing trends in observed and modelled climate
945 extremes over Australia in relation to future projections. Int J Clim 29:417-435

946

947 Alves O, Wang G, Zhong A, Smith N, Tzeitkin F, Warren G, Schiller A, Godfrey S, Meyers
948 G (2003) POAMA: Bureau of Meteorology Operational Coupled Model Forecast System.
949 In: Proceedings of national drought forum, Brisbane, April 2003, pp 49-56. Available from
950 DPI Publications, Department of Primary Industries, GPO Box 46, Brisbane, Qld 4001,
951 Australia

952

953 Arblaster JM, Alexander LV (2012) The impact of the El Niño southern oscillation on
954 maximum temperature extremes. Geophys Res Lett 39:L20702.
955 doi:10.1029/2012GL053409

956

957 Ashok K, Behera S, Rao S, Weng H, Yamagata T (2007) El Niño Modoki and its possible
958 teleconnection. J Geophys Res 112:C11007. doi:10.1029/2006JC003798

959

960 Best MJ, Pryor M, Clark DB, Rooney GG, Essery RLH, Ménard CB, Edwards JM, Hendry
961 MA, Porson A, Gedney N, Mercado LM, Sitch S, Blyth E, Boucher O, Cox PM, Grimmond
962 CSB, Harding RJ (2011) The Joint UK Land Environment Simulator (JULES), model
963 description – Part 1: Energy and water fluxes. Geosci Mod Dev 4:677-699
964
965 Blanchi R, Lucas C, Leonard J, Finkele K (2010) Meteorological conditions and wildfire-
966 related house loss in Australia. International Journal of Wildland Fire 19:914-926
967
968 Bradstock RA (2010) A biogeographic model of fire regimes in Australia: current and
969 future implications. Global Ecology and Biogeography 19:145-158
970
971 Brunet G, Shapiro M, Hoskins B, Moncrieff M, Dole R, Kiladis GN, Kirtman B, Lorenc
972 A, Mills B, Morss R, Polavarapu S, Rogers D, Schaake J, Shukla J (2010) Collaboration
973 of the Weather and Climate Communities to Advance Subseasonal-to-Seasonal Prediction.
974 Bull Amer Meteor Soc 91:1397-1406
975
976 Bureau of Meteorology (2019a) Monthly Weather Review – Australia – January 2019.
977 http://www.bom.gov.au/climate/mwr/aus/mwr-aus-201901.pdf
978
979 Bureau of Meteorology (2019b) Severe fire weather conditions in southeast Queensland
980 and northeast New South Wales in September 2019. Special Climate Statement 71, 1-35,
981 http://www.bom.gov.au/climate/current/statements/scs71.pdf
982

983 Bureau of Meteorology (2019c) Dangerous bushfire weather in spring 2019. Special
984 Climate Statement 72, 1-28, http://www.bom.gov.au/climate/current/statements/scs72.pdf
985
986 Bureau of Meteorology (2019d) Operational Implementation of ACCESS-S1 Forecast
987 Post-Processing. Operations Bulletin Number 124, Bureau National Operations Centre,
988 Melbourne. http://www.bom.gov.au/australia/charts/bulletins/opsull-124-ext.pdf
989
990 Bureau of Meteorology (2020) Extreme heat and fire weather in December 2019 and
991 January 2020. Special Climate Statement 73, 1-17.
992 http://www.bom.gov.au/climate/current/statements/scs73.pdf
993
994 Cai W, van Rensch P, Cowan T, Sullivan A (2010) Asymmetry in ENSO teleconnection
995 with regional rainfall, its multidecadal variability, and impact. J Clim 23:4944-4955
996
997 Casati B, Wilson LJ, Stephenson DB, Nurmi P, Ghelli A, Pocernich M, Damrath U, Ebert
998 EE, Brown BG, Mason S (2008) Forecast verification: current status and future directions.
999 Meteorol Appl 15:3-18
1000
1001 Christensen JH, Kumar KK, Aldrian E, An S-I, Cavalcanti IFA, de Castro M, Dong W,
1002 Goswami P, Hall A, Kanyanga JK, Kitoh A, Kossin J, Lau N-C, Renwick J, Stephenson
1003 DB, Xie S-P, Zhou T (2013) Climate Phenomena and their Relevance for Future Regional
1004 Climate Change. In: Climate Change 2013: The Physical Science Basis. Contribution of
1005 Working Group I to the Fifth Assessment Report of the Intergovernmental Panel on

1006 Climate Change [Stocker TF, Qin D, Plattner G-K, Tignor M, Allen SK, Boschung J,
1007 Nauels A, Xia Y, Bex V, Midgley PM (eds)]. Cambridge University Press, Cambridge,
1008 United Kingdom and New York, NY, US.
1009
1010 Chung CTY, Power SB (2017) The non-linear impact of El Niño, La Niña and the Southern
1011 Oscillation on seasonal and regional Australian precipitation. J Southern Hem Earth Sys
1012 Sci 67:25-45
1013
1014 Clarke H, Lucas C, Smith P (2013) Changes in Australian fire weather between 1973 and
1015 2010. International Journal of Climatology 33:931-944
1016
1017 Coughlan M (1983) A comparative climatology of blocking action in the two hemispheres.
1018 Aust Met Mag 31:3-13
1019
1020 CSIRO and Bureau of Meteorology (2015) Climate Change in Australia Information for
1021 Australia's Natural Resource Management Regions: Technical Report, CSIRO and Bureau
1022 of Meteorology, Australia.
1023 https://www.climatechangeinaustralia.gov.au/media/ccia/2.1.6/cms_page_media/168/CCI
1024 A_2015_NRM_TechnicalReport_WEB.pdf
1025
1026 CSIRO and Bureau of Meteorology (2020) State of the Climate 2020: Report, CSIRO and
1027 Bureau of Meteorology, Australia.
1028 http://www.bom.gov.au/state-of-the-climate/documents/State-of-the-Climate-2020.pdf

de Burgh-Day C, Griffiths M, Yan H, Young G, Hudson D, Alves O (2020) An adaptable framework for development and real time production of experimental sub-seasonal to seasonal forecast products. Bureau Research Report 042, ISBN: 978-1-925738-15-5.

Dee DP and Co-authors (2011) The ERA-Interim reanalysis: Configuration and performance of the data assimilation system. Quart J R Meteorol Soc 137:553-597

Dowdy AJ (2018) Climatological variability of fire weather in Australia. J Applied Met and Clim 57:221-234

Dowdy AJ, Pepler A (2018) Pyroconvection Risk in Australia: Climatological Changes in Atmospheric Stability and Surface Fire Weather Conditions. Geophys Res Lett 45:2005-2013

Felderhof L, Gillieson D (2006) Comparison of fire patterns and fire frequency in two tropical savanna bioregions. Austral Ecol 31:737-746

Ferro CAT, Stephenson DB (2011) Extremal Dependence indices: Improved Verification Measures for Deterministic Forecasts of Rare Binary Events. Weather and Forecasting 26:699-713

1051 Finkele K, Mills GA, Beard G, Jones DA (2006) National gridded drought factors and
1052 comparison of two soil moisture deficit formulations used in prediction of Forest Fire
1053 Danger Index in Australia. Aust Met Mag 55:183-197
1054
1055 Griffiths D (1999) Improved formula for the drought factor in McArthur's Forest fire
1056 danger meter. Aust For 62:202-206
1057
1058 Grose MR, Pook MJ, McIntosh PC, Risbey JS, Bindoff NL (2012) The simulation of cutoff
1059 lows in a regional climate model: reliability and future trends. Climate Dynamics 39:445-
1060 459
1061
1062 Haiden T, Duffy S (2016) Use of high-density observations in precipitation verification.
1063 ECMWF Newsletter 147.
1064
1065 Harris S, Tapper N, Packham D, Orlove B, Nicholls N (2008) The relationship between
1066 the monsoonal summer rain and dry-season fire activity of northern Australia. Int J Wildl
1067 Fire 17:674-684
1068
1069 Harris S, Nicholls N, Tapper N (2014) Forecasting fire activity in Victoria, Australia, using
1070 antecedent climate variables and ENSO indices. Int J Wildl Fire 23:173-184
1071
1072 Harris S, Lucas C (2019) Understanding the variability of Australian fire weather between
1073 1973 and 2017. PLoS ONE 14:e0222328

1074

1075 Hendon HH, Liebmann B (1990) The intraseasonal (30–50 day) oscillation of the
1076 Australian summer monsoon. J Atmos Sci 47:2909-2924

1077

1078 Hendon HH, Thompson DWJ, Wheeler MC (2007) Australian Rainfall and Surface
1079 Temperature Variations Associated with the Southern Hemisphere Annular Mode. J Clim
1080 20:2452-2467

1081

1082 Hendon HH, Lim E-P, Arblaster JM, Anderson DLT (2013) Causes and predictability of
1083 the record wet east Australian spring 2010. Clim Dyn 42:1155-1174.

1084

1085 Hendon H, Watkins AB, Lim E-P, Young G (2019) The air above antarctica is suddenly
1086 getting warmer – here's what it means for Australia. The Conversation, September 6.
1087 https://theconversation.com/the-air-above-antarctica-is-suddenly-getting-warmer-heres-
1088 what-it-means-for-australia-123080

1089

1090 Hogan RJ, Mason IB (2012) Deterministic forecasts of binary events. In Forecast
1091 verification: a practitioner's guide in atmospheric science. Jolliffe I T and Stephenson D B
1092 (eds.) 2nd Ed. Wiley. doi: 10.1002/9781119960003.ch3

1093

1094 Hudson D, Alves O, Hendon HH, Wang G (2011) The impact of atmospheric initialisation
1095 on seasonal prediction of tropical Pacific SST. Clim Dyn 36:1155-1171

1096

1097 Hudson D, Marshall A, Yin Y, Alves O, Hendon H (2013) Improving intraseasonal
1098 prediction with a new ensemble generation strategy. Mon Weather Rev 141:4429-4449
1099
1100 Hudson D, Alves O, Hendon H, Lim E-P, Liu G, Luo J-J, MacLachlan C, Marshall AG,
1101 Shi L, Wang G, Wedd R, Young G, Zhao M, Zhou X (2017) ACCESS-S1: The new Bureau
1102 of Meteorology multi-week to seasonal prediction system. J Southern Hem Earth Sys Sci
1103 67:132-159
1104
1105 Jones PA (1991) Historical records of cloud cover and climate for Australia. Aust Meteor
1106 Mag, 39:181-189
1107
1108 Jones DA, Trewin BC (2000) On the relationships between the El Niño-Southern
1109 Oscillation and Australian land surface temperature. Int J Climatol 20:697-719
1110
1111 Jones DA, Wang W, Fawcett R (2009) High-quality spatial climate data-sets for Australia.
1112 Aust Meteorol Oceanogr J 58:233-248
1113
1114 Kalnay E, Kanamitsu M, Kistler R, Collins W, Deaven D, Gandin L, Iredell M, Saha S,
1115 White G, Woollen J, Zhu Y, Leetmaa A, Reynolds B, Chelliah M, Ebisuzaki W, Higgins
1116 W, Janowiak J, Mo KC, Ropelewski C, Wang J, Jenne R, Joseph D (1996) The
1117 NCEP/NCAR 40-Year Reanalysis Project. Bull Am Meteorol Soc 77:437-471
1118

1119 Keetch JJ, Byram GM (1968) A drought index for forest fire control. USDA Forest Service
1120 Research Paper SE-38
1121
1122 Kenyon J, Hegerl GC (2008) Influence of modes of climate variability on global
1123 temperature extremes. J Clim 21:3872-3889
1124
1125 Khaykin S, Legras B, Bucci S, Sellitto P, Isaksen L, Tencé F, Bekki S, Bourassa A, Rieger
1126 L, Zawada D, Jumelet J, Godin-Beekmann S (2020) The 2019/20 Australian wildfires
1127 generated a persistent smoke-charged vortex rising up to 35 km altitude. Comm Earth &
1128 Env 1:22. https://doi.org/10.1038/s43247-020-00022-5
1129
1130 King AD. Alexander LV, Donat MG (2013) Asymmetry in the response of eastern
1131 Australia extreme rainfall to low- frequency Pacific variability. Geophys Res Lett
1132 40:2271-2277.
1133
1134 Lim E-P, Hendon HH, Rashid H (2013) Seasonal predictability of the Southern Annular
1135 Mode due to its association with ENSO. J Clim 26:8037-8054
1136
1137 Lim E-P, Hendon HH, Hudson D, Zhao M, Shi L, Alves O, Young G (2016) Evaluation of
1138 the ACCESS-S1 hindcasts for prediction of Victorian seasonal rainfall. Bureau Research
1139 Report No. 19. http://www.bom.gov.au/research/research-reports.shtml
1140

1141 Lim E-P, Hendon HH, Boschat G, Hudson D, Thompson DWJ, Dowdy AJ, Arblaster JM
1142 (2019) Australian hot and dry extremes induced by weakenings of the stratospheric polar
1143 vortex. Nat Geo 12:896-901
1144
1145 Lim E-P, Hendon HH, Shi L, de Burgh-Day C, Hudson D, King A, Trewin B, Griffiths M,
1146 Marshall AG (2020) Tropical forcing of Australian extreme low minimum temperatures in
1147 September 2019. In press.
1148
1149 Long M (2006) A climatology of extreme fire weather days in Victoria. Aust Meteor Mag
1150 55:3-18
1151
1152 Love G, Downey A (1986) The prediction of bushfires in central Australia. Aust Meteor
1153 Mag 34:93-101.
1154
1155 Lucas C, Hennessy K, Mills G, Bathols J (2007) Bushfire weather in south-east Australia:
1156 recent trends and projected climate change impacts. Bushfire CRC and CSIRO, Melbourne
1157
1158 Lucas C (2010) On developing a historical fire weather data-set for Australia. Aust
1159 Meteorol Oceanogr J 60:1-14
1160
1161 MacLachlan C, Arribas A, Peterson KA, Maidens A, Fereday D, Scaife AA, Gordon M,
1162 Vellinga M, Williams A, Comer RE, Camp J, Xavier P, Madec G (2015) Global seasonal

1163 forecast system version 5 (GloSea5): a high-resolution seasonal forecast system. Q J R
1164 Meteorol Soc 141:1072-1084
1165
1166 Madden RA, Julian PR (1994) Observations of the 40–50 day tropical Oscillation - a
1167 review. Mon Wea Rev 122:814-837
1168
1169 Mariani M, Fletcher MS, Holz A, Nyman P (2016) ENSO controls interannual fire activity
1170 in southeast Australia. Geophys Res Lett 43:10891-10900
1171
1172 Marshall AG, Hudson D, Wheeler MC, Hendon HH, Alves O (2012) Simulation and
1173 prediction of the Southern Annular Mode and its influence on Australian intra-seasonal
1174 climate in POAMA. Clim Dyn 38:2483-2502
1175
1176 Marshall AG, Hudson D, Hendon HH, Pook MJ, Alves O, Wheeler MC (2014a) Simulation
1177 and prediction of blocking in the Australian region and its influence on intra-seasonal
1178 rainfall in POAMA-2. Clim Dyn, 42:3271-3288
1179
1180 Marshall AG, Hudson D, Wheeler MC, Alves O, Hendon HH, Pook MJ, Risbey JS (2014b)
1181 Intra-seasonal drivers of extreme heat over Australia in observations and POAMA-2. Clim
1182 Dyn 43:1915-1937
1183

1184 Marshall AG, Hendon HH, Hudson D (2020) Influence of the Madden-Julian Oscillation
1185 on multiweek prediction of Australian rainfall extremes using the ACCESS-S1 prediction
1186 system. J Southern Hem Earth Sys Sci, submitted
1187
1188 Matthews S, Fox-Hughes P, Grootemaat S, Hollis JJ, Kenny BJ, Sauvage S (2018) National
1189 Fire Danger Rating System: Research Prototype. NSW Rural Fire Service, Lidcombe,
1190 NSW, 384 pp.
1191
1192 McArthur AG (1967) Fire Behaviour in Eucalypt Forests. Department of National
1193 Development Forestry and Timber Bureau, Canberra, Leaflet 107.
1194
1195 Meyers G, McIntosh P, Pigot L, Pook M (2007) The years of El Niño, La Niña, and
1196 interactions with the tropical Indian Ocean. J Clim 20:2872-2880
1197
1198 Min S-K, Cai W, Whetton P (2013) Influence of climate variability on seasonal extremes
1199 over Australia. J Geophys Res Atmos 118:643-654
1200
1201 Mogensen K, Balmaseda M, Weaver AT, Martin M, Vidard A (2009) NEMOVAR: A
1202 variational data assimilation system for the NEMO ocean model. In: ECMWF Newsletter.
1203 Walter Z. (ed.) 120:17–21. ECMWF Reading UK
1204

1205 Mogensen K, Balmaseda MA, Weaver AT (2012) The NEMOVAR ocean data assimilation
1206 system as implemented in the ECMWF ocean analysis for Sys-tem 4. Tech Rep TR-
1207 CMGC-12-30. CERFACS Toulouse France
1208
1209 NASA (2020) Studying the 2019-2020 Australian bushfires using NASA data.
1210 https://storymaps.arcgis.com/stories/9ebbe1b54dc847f2a7dd01917c9f3071
1211
1212 Nicholls N, Lavery B, Frederiksen C, Drosdowsky W, Torok S (1996) Recent apparent
1213 changes in relationships between the El Niño-Southern Oscillation and Australian rainfall
1214 and temperature. Geophys Res Lett 23:3357-3360
1215
1216 Nicholls N, Drosdowsky W, Lavery B (1997) Australian rainfall variability and change.
1217 Weather 52:66-72
1218
1219 Nicholls N, Lucas C (2007) Interannual variations of area burnt in Tasmanian bushfires:
1220 Relationships with climate and predictability. Int J Wildl Fire 16:540-546
1221
1222 Noble IR, Bary GAV, Gill AM (1980) McArthur's fire-danger meters expressed as
1223 equations. Aust J Ecology 5:201-203
1224
1225 North R, Truman M, Mittermaier M, Rodwell MJ (2013) An assessment of the SEEPS and
1226 SEDI metrics for the verification of 6 h forecast precipitation accumulations. Meteor
1227 Applic 20:164-175

1228

1229 Ohneiser K, Ansmann A, Baars H, Seifert P, Barja B, Jimenez C, Radenz M, Teisseire A,
1230 Floutsi A, Haarig M, Foth A, Chudnovsky A, Engelmann R, Zamorano F, Bühl J,
1231 Wandinger U (2020) Smoke of extreme Australian bushfires observed in the stratosphere
1232 over Punta Arenas, Chile, in January 2020: optical thickness, lidar ratios, and
1233 depolarization ratios as 355 and 532 nm. Atmos Chem Phys 20:8003-8015

1234

1235 Perkins SE, Alexander LV, Nairn JR (2012) Increasing frequency, intensity and duration
1236 of observed heatwaves and warm spells. Geophys Res Lett 39:L20714.
1237 doi:10.1029/2012GL053361

1238

1239 Pook MJ, Gibson T (1999) Atmospheric blocking and storm tracks during SOP-1 of the
1240 FROST Project. Aust Meteor Mag 48:51-60

1241

1242 Pook MJ, McIntosh PC, Meyers GA (2006) The synoptic decomposition of cool-season
1243 rainfall in the Southeastern Australian cropping region. J Appl Meteor Climatol 45:1156-
1244 1170

1245

1246 Pook MJ, Risbey J, McIntosh P, Ummenhofer C, Marshall AG, Meyers GA (2013) The
1247 seasonal cycle of blocking and associated physical mechanisms in the Australian region
1248 and relationship with rainfall. Mon Weather Rev 141:4534-4553

1249

1250 Power S, Tseitkin F, Torok SJ, Lavery B, Dahni R, McAvaney B (1998) Australian
1251 temperature, Australian rainfall and the Southern Oscillation, 1910–1992: coherent
1252 variability and recent changes. Aust Meteor Mag 47:85-101
1253
1254 Power S, Haylock M, Colman R, Wang X (2006) The predictability of interdecadal
1255 changes in ENSO activity and ENSO teleconnections. J Clim 19:4755-4771
1256
1257 Rae JGL, Hewitt HT, Keen AB, Ridley JK, West AE, Harris CM, Hunke EC, Walters DN
1258 (2015) Development of the Global Sea Ice 6.0 CICE configuration for the Met Office
1259 Global Coupled Model. Geosci Model Dev 8:2221-2230
1260
1261 Rashid H, Hendon HH, Wheeler M, Alves O (2011) Prediction of the Madden-Julian
1262 Oscillation with the POAMA dynamical seasonal prediction system. Clim Dyn 36:649-661
1263
1264 Reynolds RW, Smith TM (1994) Improved Global Sea Surface Temperature Analyses
1265 Using Optimum Interpolation. J Clim 7:929-948
1266
1267 Risbey JS, Pook MJ, McIntosh PC, Wheeler MC, Hendon HH (2009) On the Remote
1268 Drivers of Rainfall Variability in Australia. Mon Weather Rev 137:3233-3253
1269
1270 Saji NH, Goswami BN, Vinayachandran PN, Yamagata T (1999) A dipole mode in the
1271 tropical Indian Ocean. Nature 401:360-363
1272

1273 Scherhag R (1952) Die explosionsartigen Stratospärenerwärmungen des Spätwinters
1274 1951–1952. Ber Dtsch Wetterdienst (US Zone) 6:51-63
1275
1276 Singh H. Arora K, Ashrit R, Rajagopal EN (2017) Verification of pre-monsoon
1277 temperature forecasts over India during 2016 with a focus on heatwave prediction. Nat
1278 Hazards Earth Syst Sci 17:1469-1485.
1279
1280 Spiegel MR (1961) Schaum's outline of theory and problems of Statistics. Schaum
1281 Publishing Company, New York, 359pp
1282
1283 Stockdale TN (1997) Coupled Ocean–Atmosphere Forecasts in the Presence of Climate
1284 Drift. Mon Weather Rev 125:809-818
1285
1286 Taschetto AS, England MH (2009) El Niño Modoki Impacts on Australian Rainfall. J
1287 Clim 22:3167-3174.
1288
1289 Trenberth KE (1979) Interannual variability of the 500 mb zonal mean flow in the southern
1290 hemisphere. Mon Weather Rev 107:1515-1524
1291
1292 Verdon DC, Kiem AS, Franks SW (2004) Multi-decadal variability of forest fire risk–
1293 eastern Australia. Int J Wildl Fire 13:165-171
1294

1295 Walters D, Brooks M, Boutle I, Melvin T, Stratton R, Vosper S, Wells H, Williams K,
1296 Wood N, Allen T, Bushell A, Copsey D, Earnshaw P, Edwards J, Gross M, Hardiman S,
1297 Harris C, Heming J, Klingaman N, Levine R, Manners J, Martin G, Milton S, Mittermaier
1298 M, Morcrette C, Riddick T, Roberts M, Sanchez C, Selwood P, Stirling A, Smith C, Suri
1299 D, Tennant W, Vidale PL, Wilkinson J, Willett M, Woolnough S, Xavier P (2017) The Met
1300 Office Unified Model Global Atmosphere 6.0/6.1 and JULES Global Land 6.0/6.1
1301 configurations. Geosci Mod Dev 10:1487-1520
1302
1303 Wang G, Hendon HH (2020) Impacts of the Madden–Julian Oscillation on wintertime
1304 Australian minimum temperatures and Southern Hemisphere circulation. Clim Dyn
1305 55:3087-3099.
1306
1307 Wang G, Cai W, Yang K, Santoso A, Yamagata T (2020) A Unique Feature of the 2019
1308 Extreme Positive Indian Ocean Dipole Event. Geophys Res Lett 47:e2020GL088615
1309
1310 Wheeler MC, Hendon HH (2004) An all-season real-time multivariate MJO index:
1311 Development of an index for monitoring and prediction. Mon Weather Rev 132:1917-1932
1312
1313 Wheeler MC, Hendon HH, Cleland S, Meinke H, Donald A (2009) Impacts of the Madden–
1314 Julian Oscillation on Australian Rainfall and Circulation. J Clim 22:1482-1498
1315
1316 White CJ, Hudson D, Alves O (2014) ENSO, the IOD and the intraseasonal prediction of
1317 heat extremes across Australia using POAMA-2. Climate Dynamics 43:1791-1810

1318

1319 Williams AAJ, Karoly DJ (1999) Extreme Fire Weather in Australia and the Impact of the
1320 El Niño-Southern Oscillation. Aust Met Mag 48:15-22

1321

1322 Williams AAJ, Karoly DJ, Tapper N (2001) The sensitivity of Australian fire danger to
1323 climate change. Clim Chang 49:11-191

1324

1325 Zhou X, Luo J, Alves O, Hendon H (2015) Comparison of GLOSEA5 and POAMA2.4
1326 Hindcasts 1996-2009: Ocean Focus. Bureau Research Report No. 10.
1327 http://www.bom.gov.au/research/research-reports.shtml

Figure captions

Figure 1: 90th percentile thresholds of weekly-mean FFDI for observations (left column) and for ACCESS-S1 for lead times of 2-3 weeks (right column), in SON (top row) and DJF (bottom row).

Figure 2: Ratio of probabilities of upper decile weekly FFDI events for El Niño in SON (top row) and DJF (second row), and for La Niña in SON (third row) and DJF (bottom row), for observations (left column) and ACCESS-S1 at lead times of 2-3 weeks (right column). Ratios are calculated relative to the mean decile probability (nominally 0.1), and bold contours indicate regions where the ratio is significantly different from one at 95% confidence using a z-score test for event probabilities. The sample size *n* is indicated for each figure panel.

Figure 3: Same as Figure 2 but for the positive IOD phase (top row) and negative IOD (bottom row) in SON.

Figure 4: Same as Figure 2 but for the high SAM phase in SON (top row) and DJF (second row), and for the low SAM phase in SON (third row) and DJF (bottom row).

Figure 5: Same as Figure 2 but for MJO phases 1 (top row) to 4 (bottom row) in SON.

Figure 6: Same as Figure 2 but for MJO phases 5 (top row) to 8 (bottom row) in SON.

Figure 7: Same as Figure 2 but for MJO phases 1 (top row) to 4 (bottom row) in DJF.

Figure 8: Same as Figure 2 but for MJO phases 5 (top row) to 8 (bottom row) in DJF.

Figure 9: Same as Figure 2 but for high split-flow blocking activity at 140°E in SON (top row) and DJF (second row), and for low split-flow blocking activity at 140°E in SON (third row) and DJF (bottom row).

Figure 10: Same as Figure 2 but for high STRH activity in SON (top row) and DJF (second row), and for low STRH activity in SON (third row) and DJF (bottom row).

Figure 11: SEDI skill scores for ACCESS-S1 forecasts of upper decile weekly FFDI events in SON (left) and DJF (right) at target lead times of weeks 2 and 3 combined. Unshaded (white) areas indicate where skill scores are not significantly different from zero at 95% confidence using the SEDI standard error.

Figure 12: SEDI skill scores for ACCESS-S1 forecasts of upper decile weekly FFDI events for El Niño (left column) and La Niña (right column) in SON (top row) and DJF (bottom row), shown as differences from when ENSO is weak, at target lead times of weeks 2 and 3 combined. Unshaded (white) areas indicate where skill scores are not significantly different from zero at 95% confidence using the SEDI standard error.

Figure 13: Same as Figure 12 but for the positive (left) and negative (right) IOD phase in SON, shown as differences from when the IOD is weak.

Figure 14: Same as Figure 12 but for the high (left column) and low (right column) SAM phase in SON (top row) and DJF (bottom row), shown as differences from when the SAM is weak.

Figure 15: Same as Figure 12 but for MJO phases 1-8 in SON, shown as differences from when the MJO is weak.

Figure 16: Same as Figure 12 but for MJO phases 1-8 in DJF, shown as differences from when the MJO is weak.

Figure 17: Same as Figure 12 but for high (left column) and low (right column) split-flow blocking activity at 140°E in SON (top row) and DJF (bottom row), shown as differences from when split-flow blocking activity is weak.

Figure 18: Same as Figure 12 but for high (left column) and low (right column) STRH activity in SON (top row) and DJF (bottom row), shown as differences from when STRH activity is weak.

Figure 19: Each map shows the climate driver with the highest probability of upper decile weekly FFDI at each grid point in SON (top row) and DJF (bottom row), for observations (left column) and ACCESS-S1 at lead times of 2-3 weeks (right column).

Figure

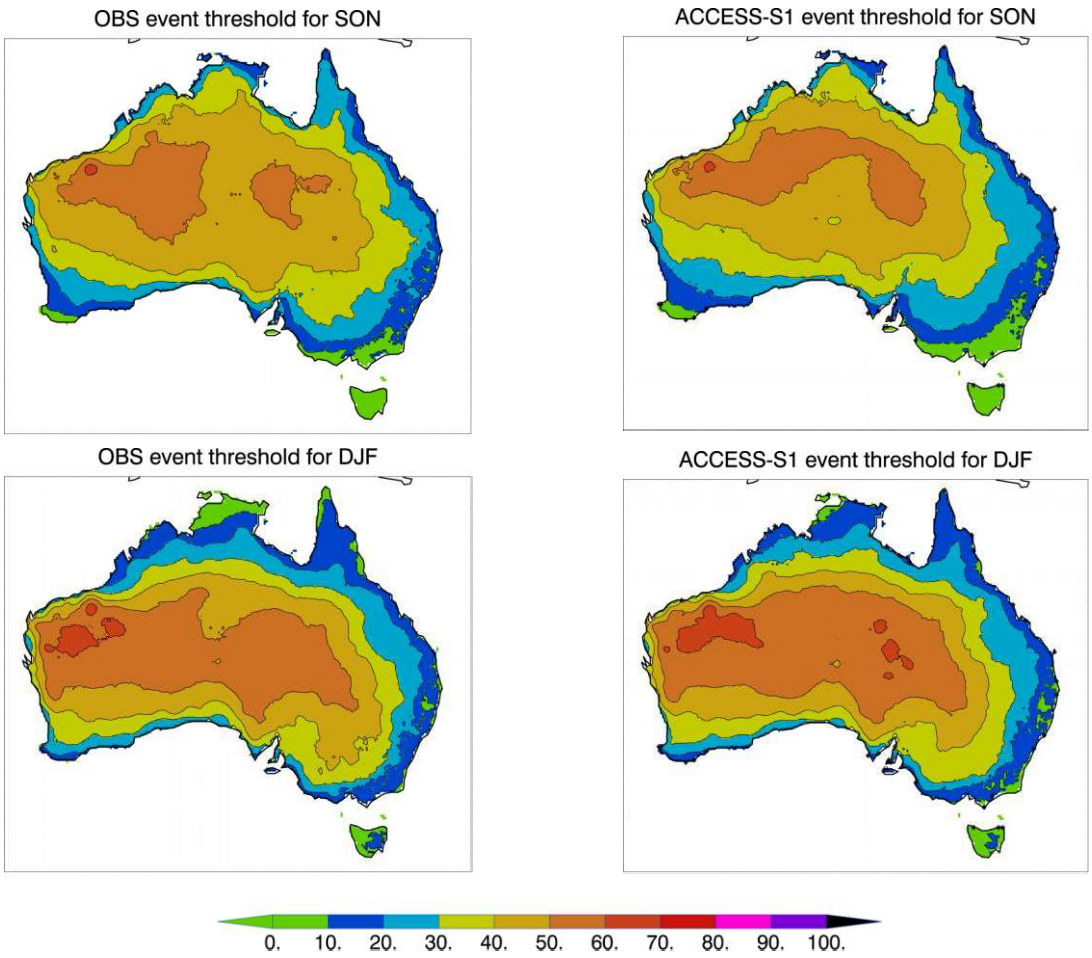

Figure 1: 90th percentile thresholds of weekly-mean FFDI for observations (left column) and for ACCESS-S1 for lead times of 2-3 weeks (right column), in SON (top row) and DJF (bottom row).

OBS El Nino SON (n=53)

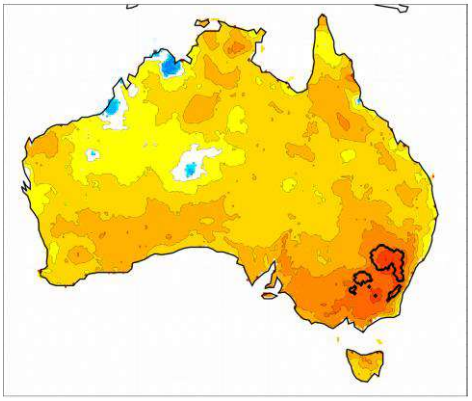

ACCESS-S1 El Nino SON (n=765)

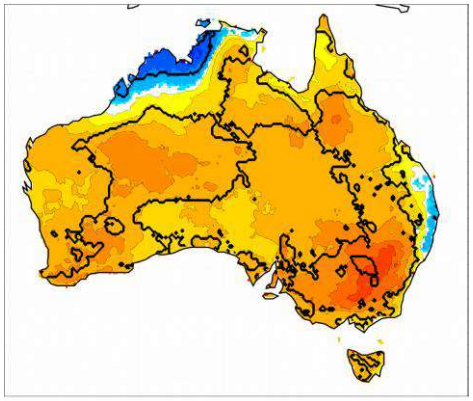

OBS El Nino DJF (n=74)

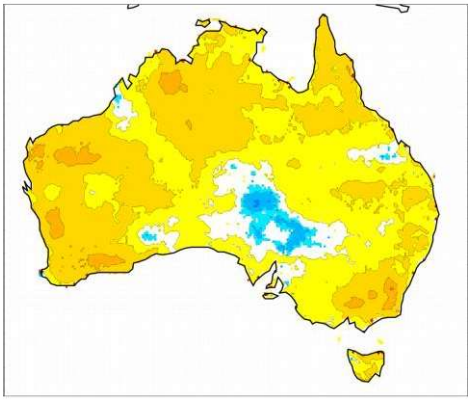

ACCESS-S1 El Nino DJF (n=1088)

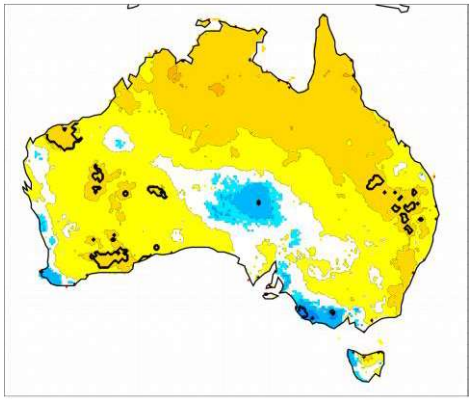

OBS La Nina SON (n=63)

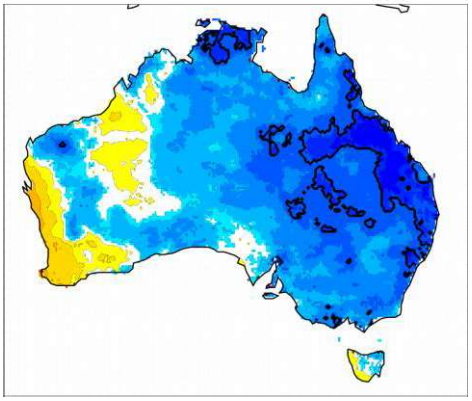

ACCESS-S1 La Nina SON (n=834)

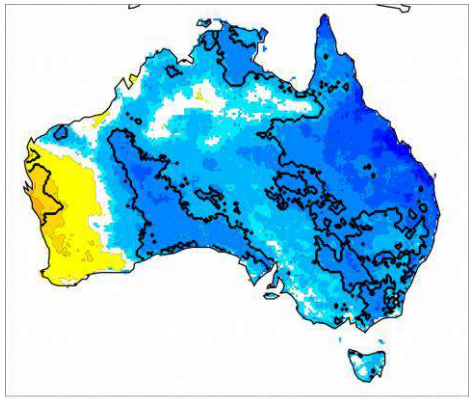

OBS La Nina DJF (n=75)

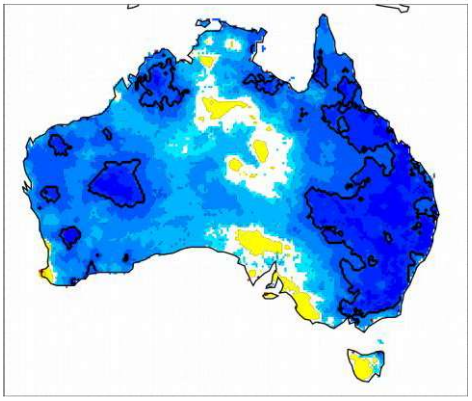

ACCESS-S1 La Nina DJF (n=970)

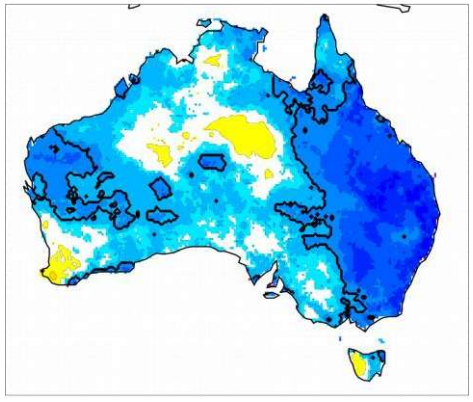

Figure 2: Ratio of probabilities of upper decile weekly FFDI events for El Niño in SON (top row) and DJF (second row), and for La Niña in SON (third row) and DJF (bottom row), for observations (left column) and ACCESS-S1 at lead times of 2-3 weeks (right column). Ratios are calculated relative to the mean decile probability (nominally 0.1), and bold contours indicate regions where the ratio is significantly different from one at 95% confidence using a z-score test for event probabilities. The sample size *n* is indicated for each figure panel.

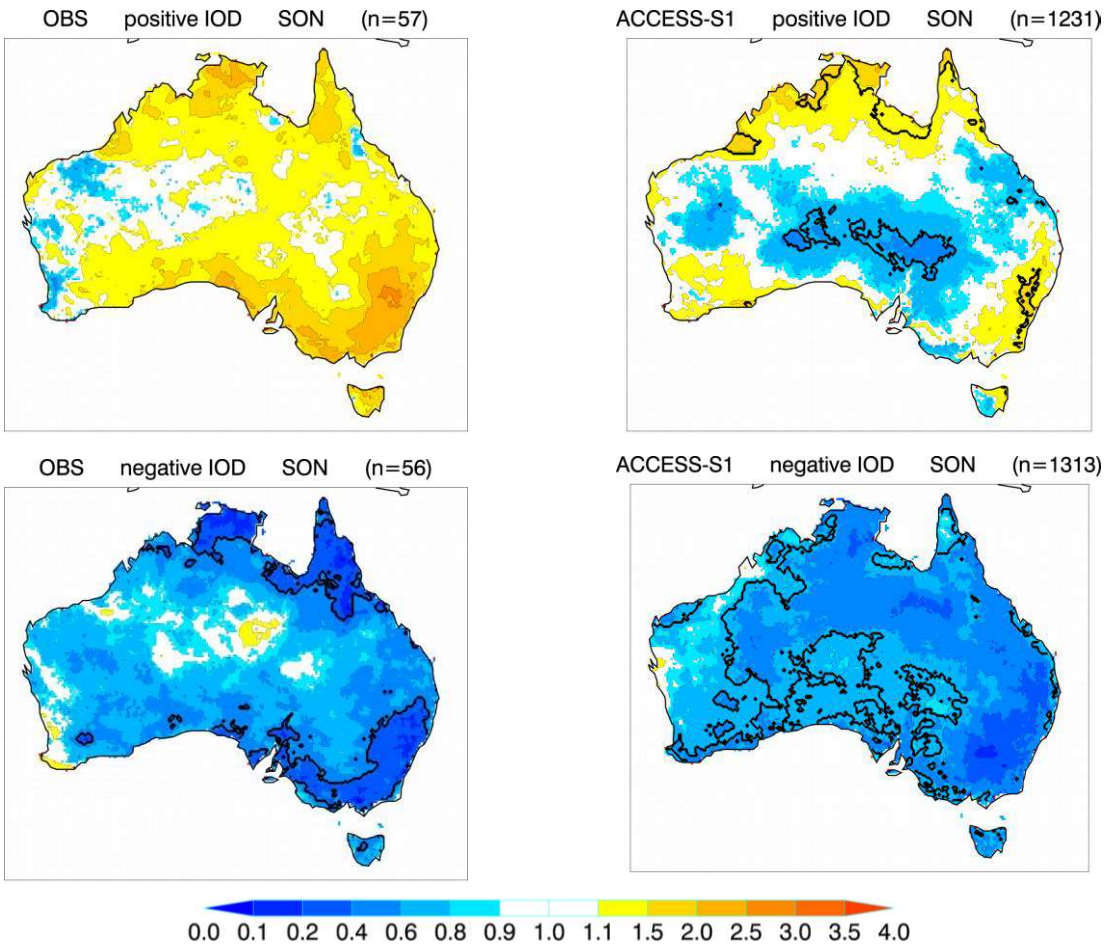

Figure 3: Same as Figure 2 but for the positive IOD phase (top row) and negative IOD (bottom row) in SON.

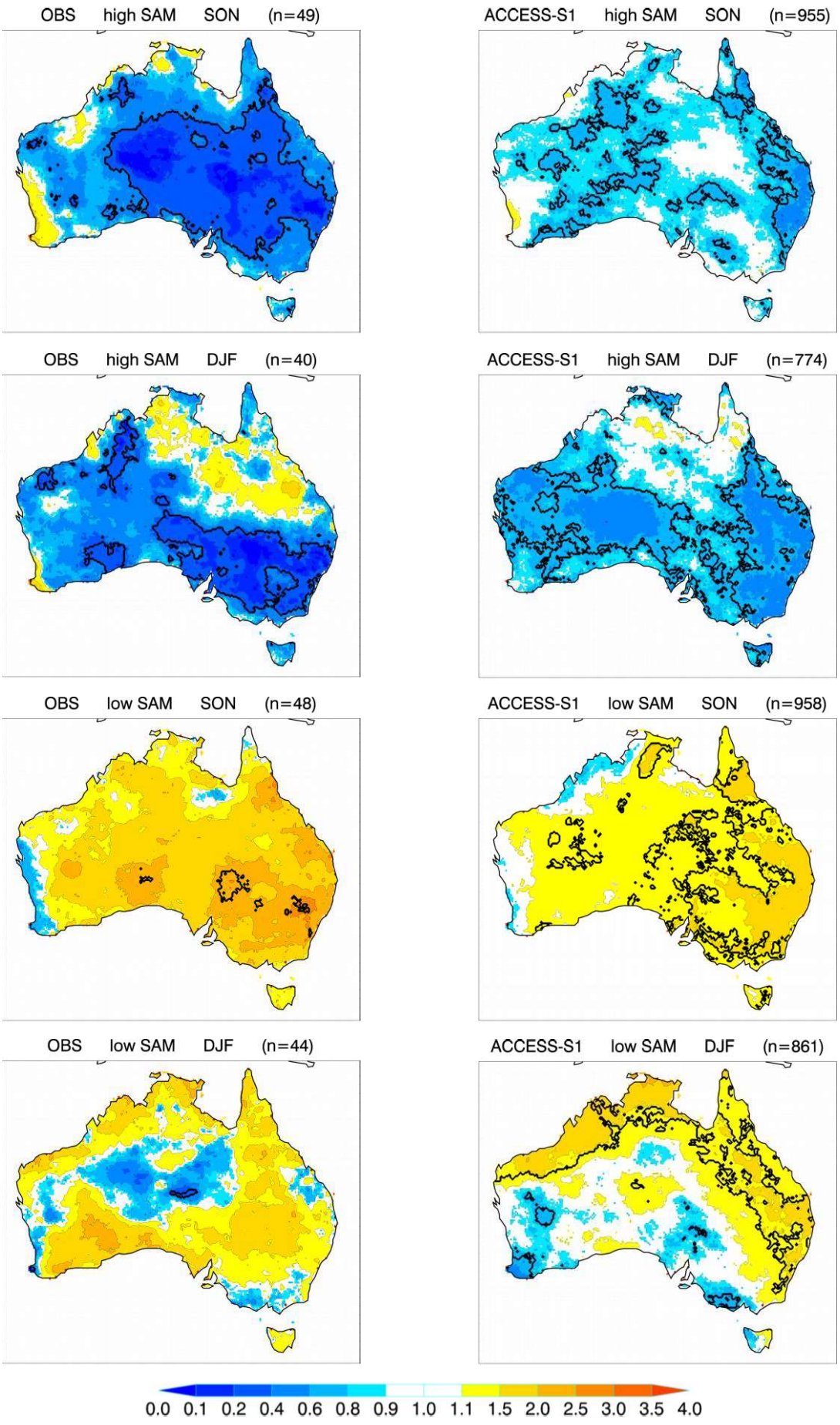
OBS high SAM SON (n=49)
ACCESS-S1 high SAM SON (n=955)
OBS high SAM DJF (n=40)
ACCESS-S1 high SAM DJF (n=774)
OBS low SAM SON (n=48)
ACCESS-S1 low SAM SON (n=958)
OBS low SAM DJF (n=44)
ACCESS-S1 low SAM DJF (n=861)
0.0 0.1 0.2 0.4 0.6 0.8 0.9 1.0 1.1 1.5 2.0 2.5 3.0 3.5 4.0

Figure 4: Same as Figure 2 but for the high SAM phase in SON (top row) and DJF (second row), and for the low SAM phase in SON (third row) and DJF (bottom row).

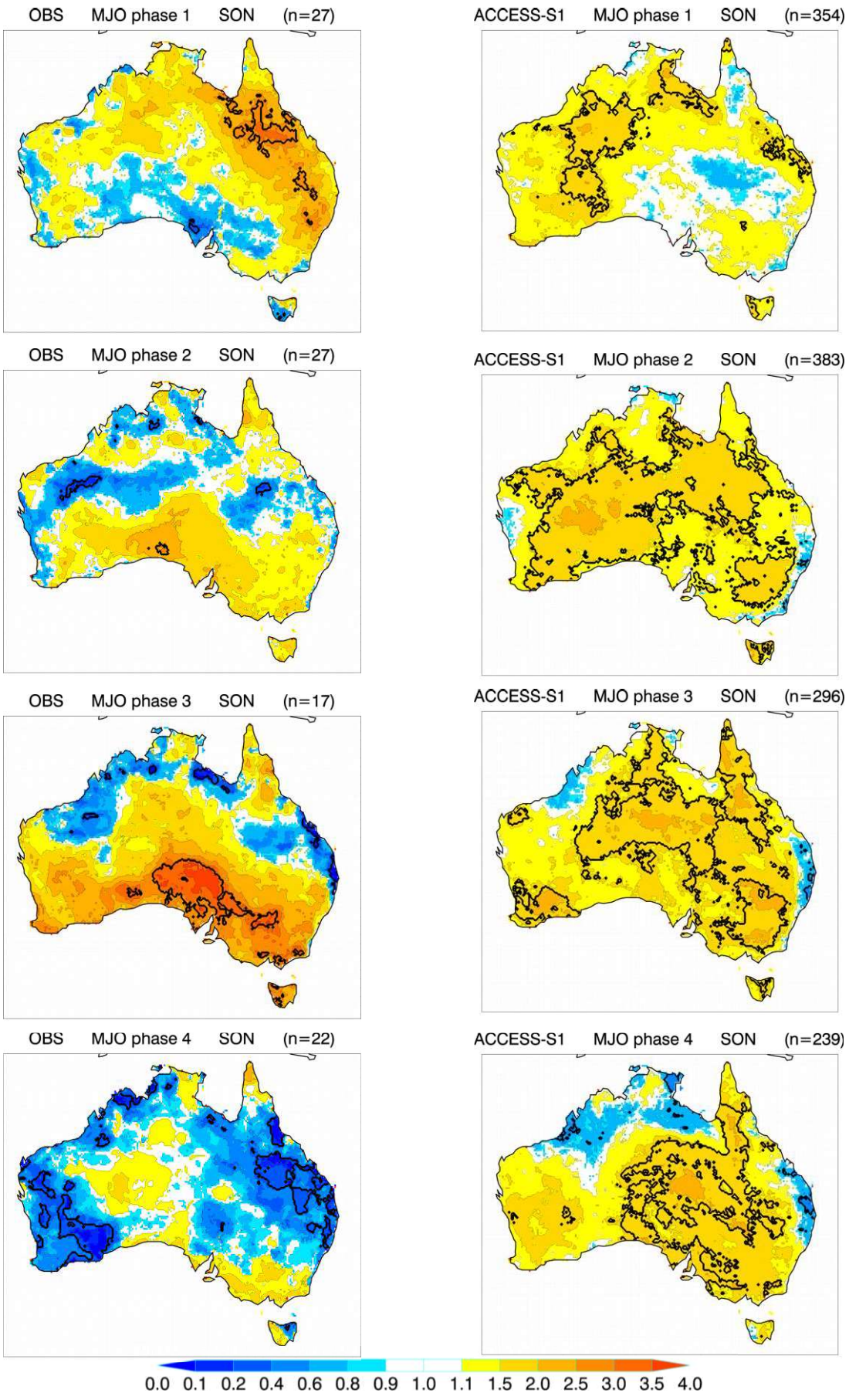

Figure 5: Same as Figure 2 but for MJO phases 1 (top row) to 4 (bottom row) in SON.

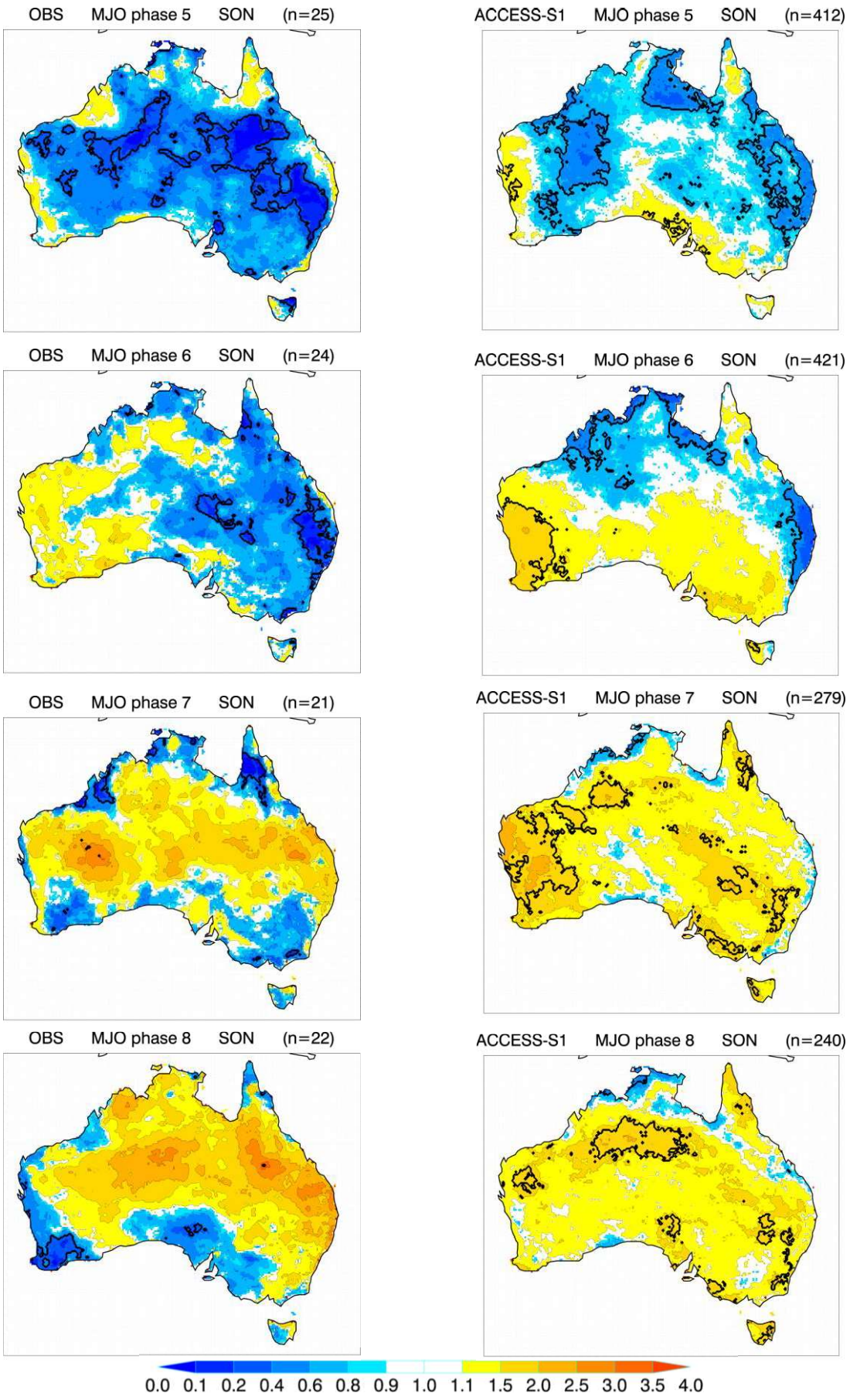

Figure 6: Same as Figure 2 but for MJO phases 5 (top row) to 8 (bottom row) in SON.

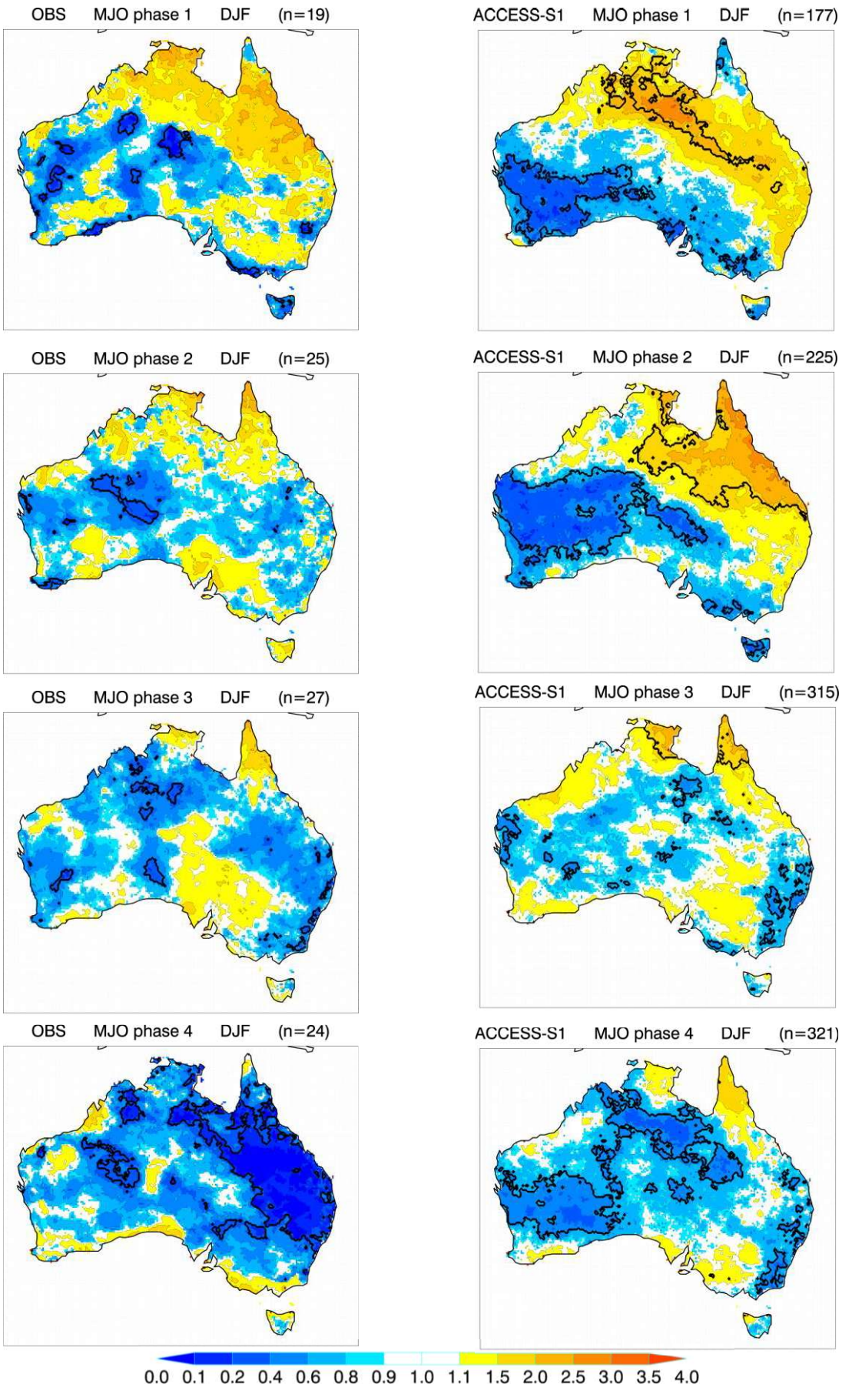

Figure 7: Same as Figure 2 but for MJO phases 1 (top row) to 4 (bottom row) in DJF.

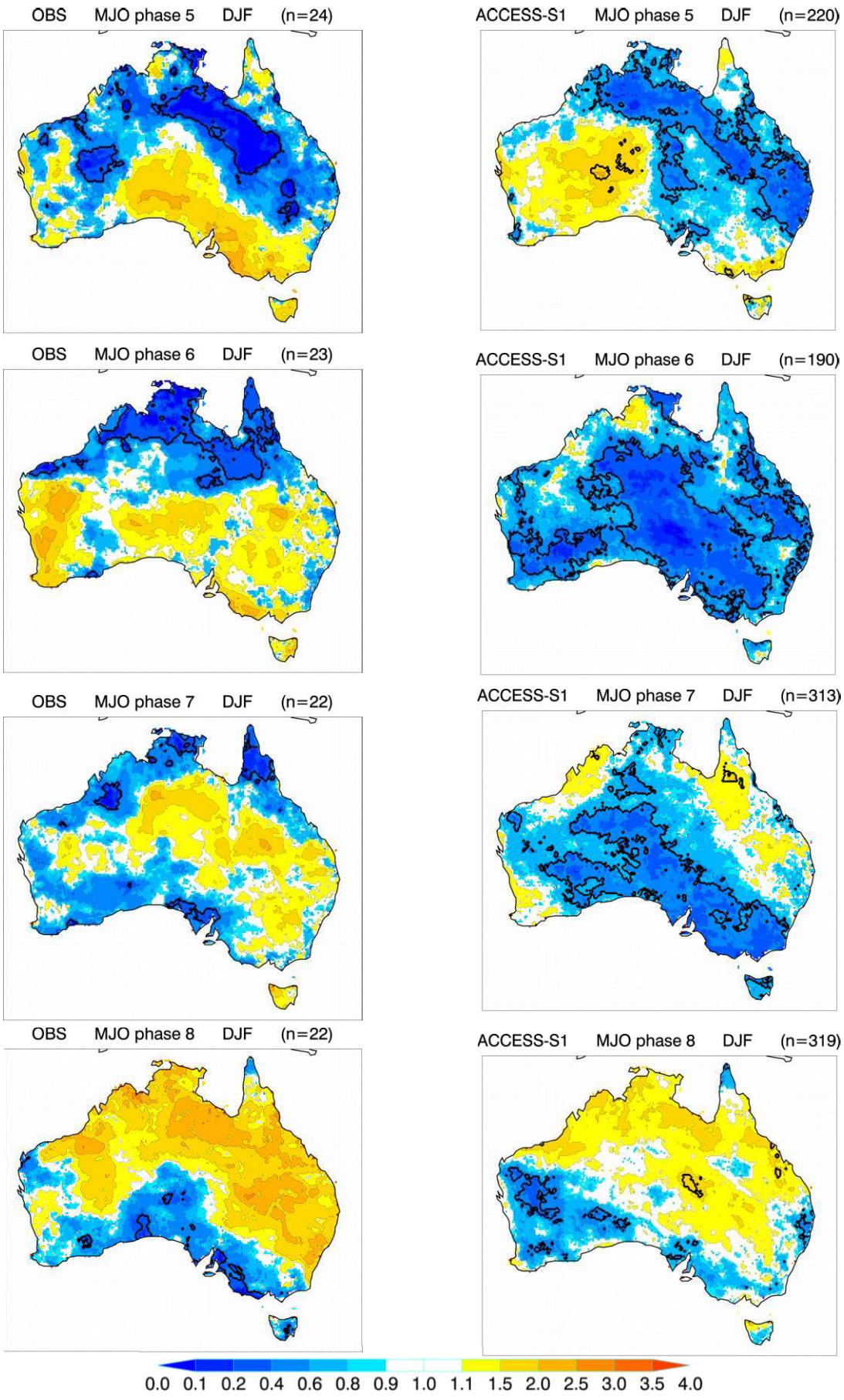

Figure 8: Same as Figure 2 but for MJO phases 5 (top row) to 8 (bottom row) in DJF.

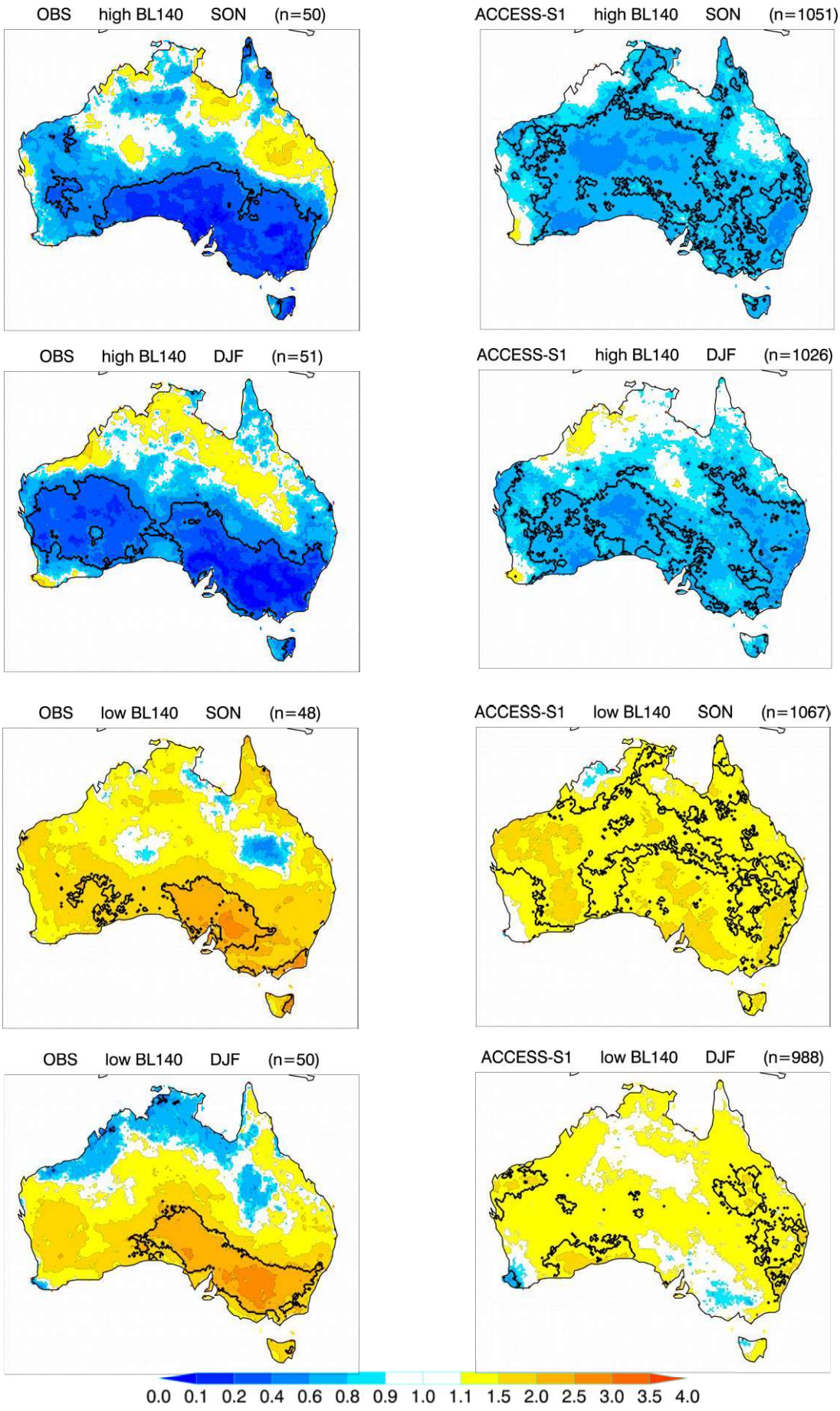
OBS high BL140 SON (n=50)
ACCESS-S1 high BL140 SON (n=1051)
OBS high BL140 DJF (n=51)
ACCESS-S1 high BL140 DJF (n=1026)
OBS low BL140 SON (n=48)
ACCESS-S1 low BL140 SON (n=1067)
OBS low BL140 DJF (n=50)
ACCESS-S1 low BL140 DJF (n=988)
0.0 0.1 0.2 0.4 0.6 0.8 0.9 1.0 1.1 1.5 2.0 2.5 3.0 3.5 4.0

Figure 9: Same as Figure 2 but for high split-flow blocking activity at 140°E in SON (top row) and DJF (second row), and for low split-flow blocking activity at 140°E in SON (third row) and DJF (bottom row).

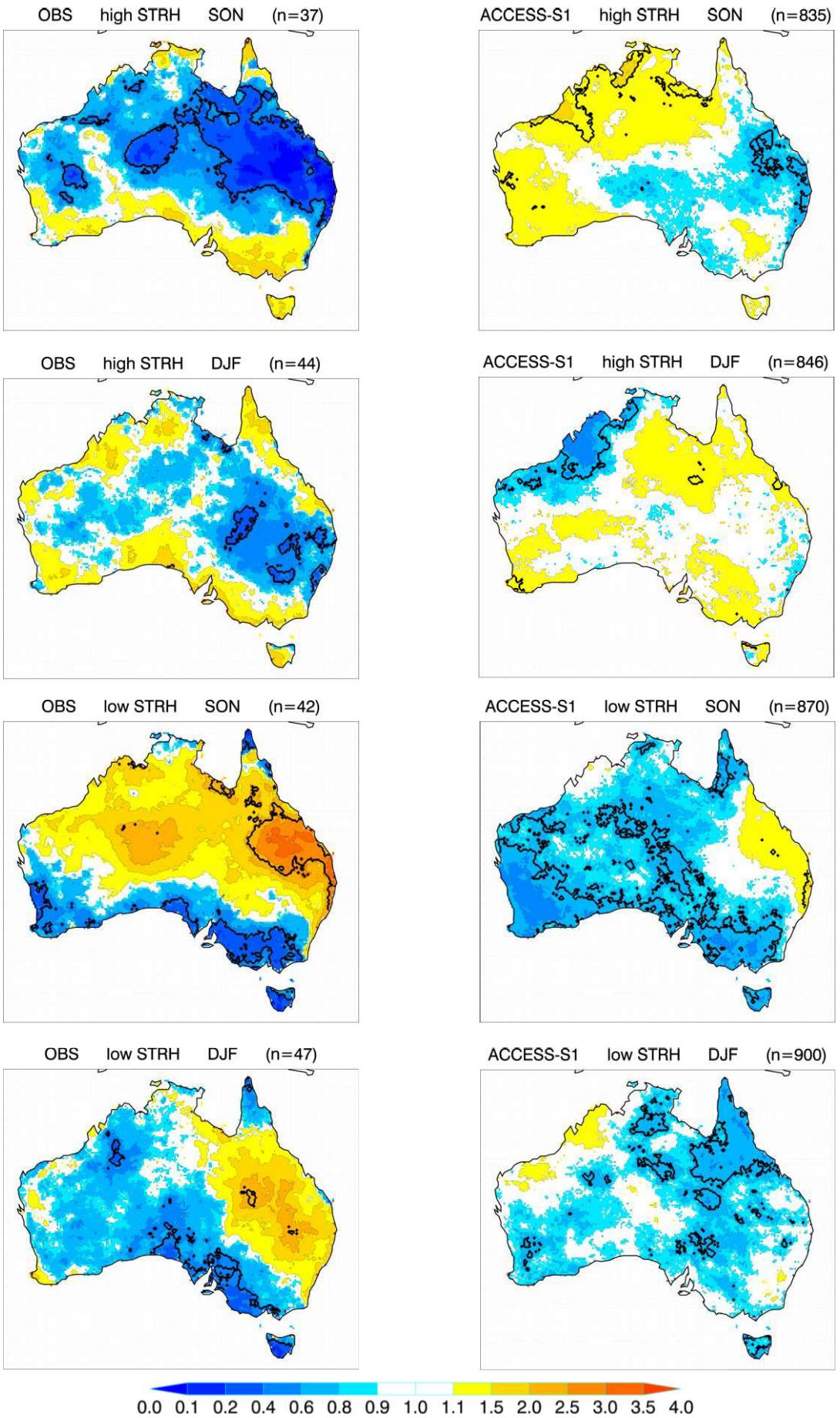
OBS high STRH SON (n=37)
ACCESS-S1 high STRH SON (n=835)
OBS high STRH DJF (n=44)
ACCESS-S1 high STRH DJF (n=846)
OBS low STRH SON (n=42)
ACCESS-S1 low STRH SON (n=870)
OBS low STRH DJF (n=47)
ACCESS-S1 low STRH DJF (n=900)
0.0 0.1 0.2 0.4 0.6 0.8 0.9 1.0 1.1 1.5 2.0 2.5 3.0 3.5 4.0

Figure 10: Same as Figure 2 but for high STRH activity in SON (top row) and DJF (second row), and for low STRH activity in SON (third row) and DJF (bottom row).

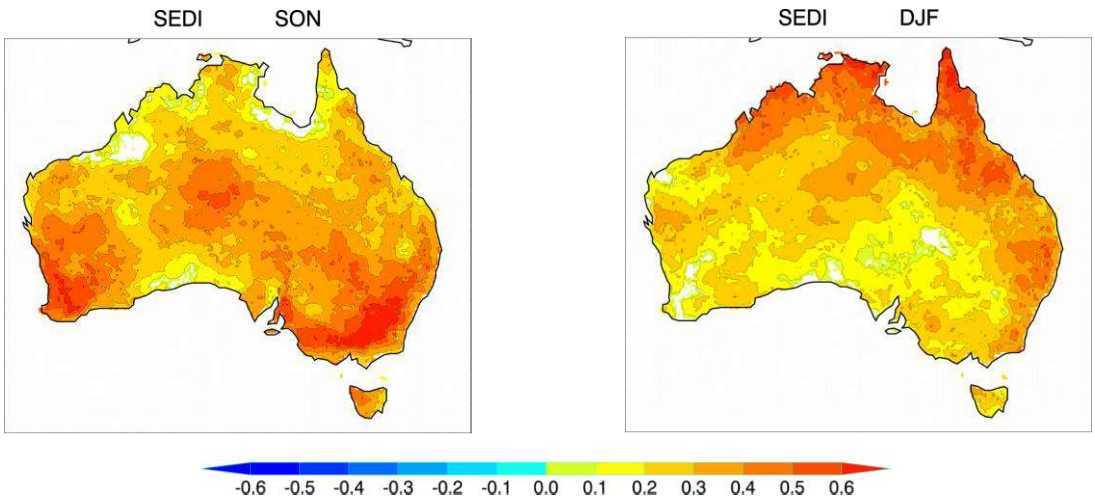

Figure 11: SEDI skill scores for ACCESS-S1 forecasts of upper decile weekly FFDI events in SON (left) and DJF (right) at target lead times of weeks 2 and 3 combined. Unshaded (white) areas indicate where skill scores are not significantly different from zero at 95% confidence using the SEDI standard error.

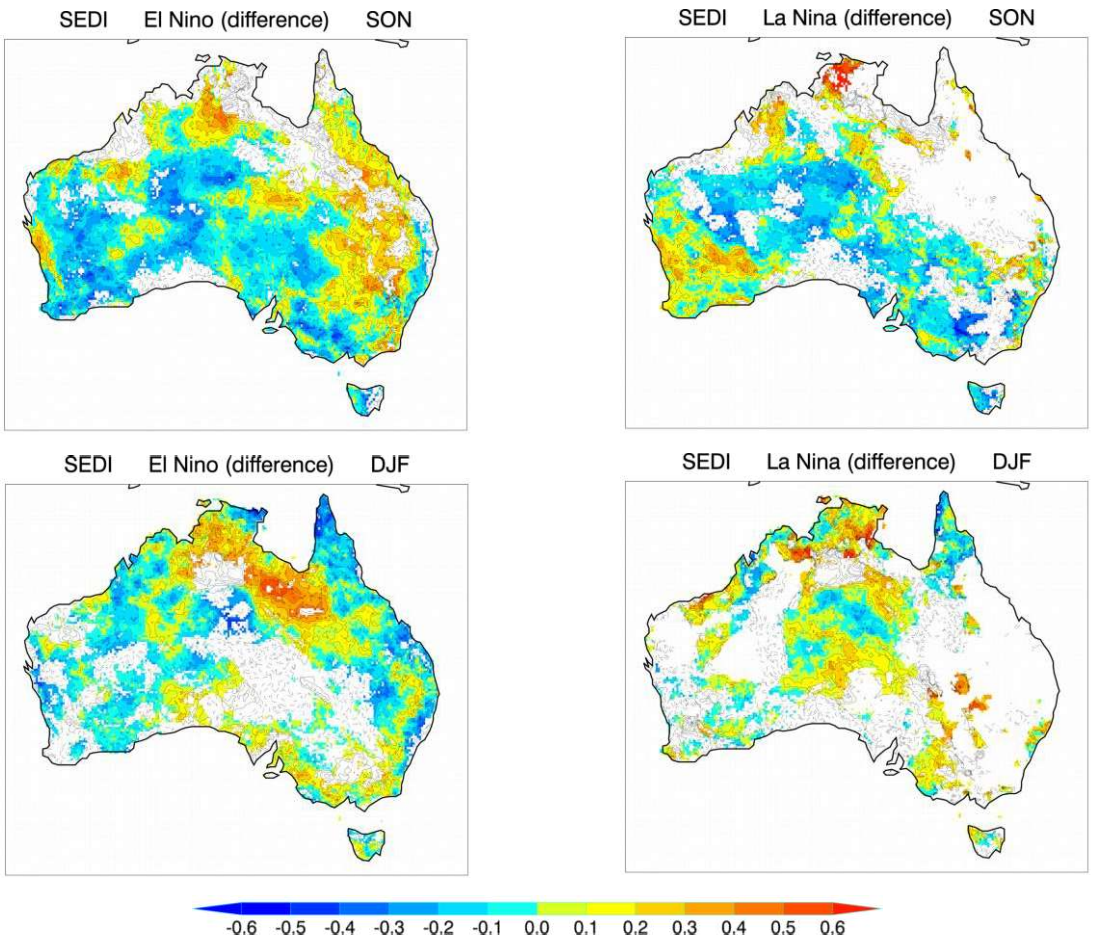

Figure 12: SEDI skill scores for ACCESS-S1 forecasts of upper decile weekly FFDI events for El Niño (left column) and La Niña (right column) in SON (top row) and DJF (bottom row), shown as differences from when ENSO is weak, at target lead times of weeks 2 and 3 combined. Unshaded (white) areas indicate where skill scores are not significantly different from zero at 95% confidence using the SEDI standard error.

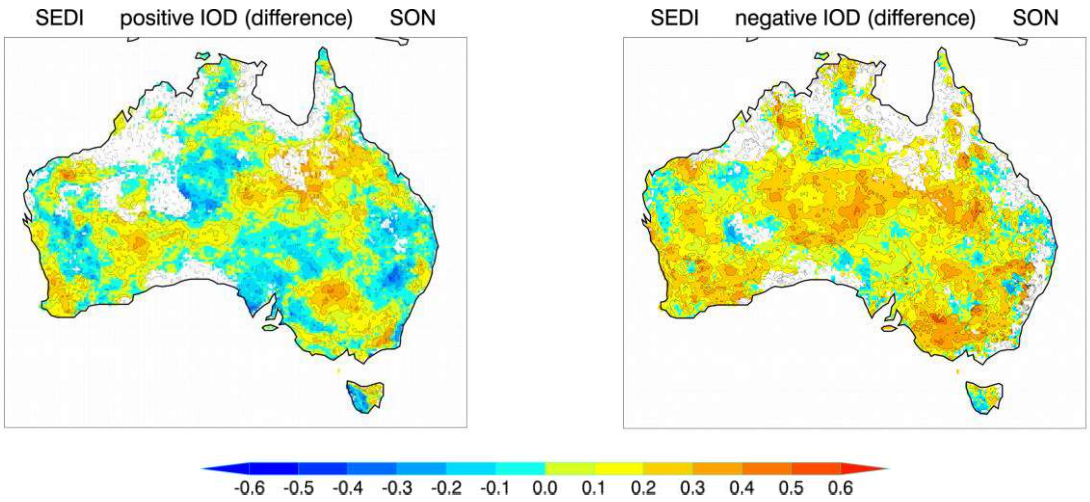

Figure 13: Same as Figure 12 but for the positive (left) and negative (right) IOD phase in SON, shown as differences from when the IOD is weak.

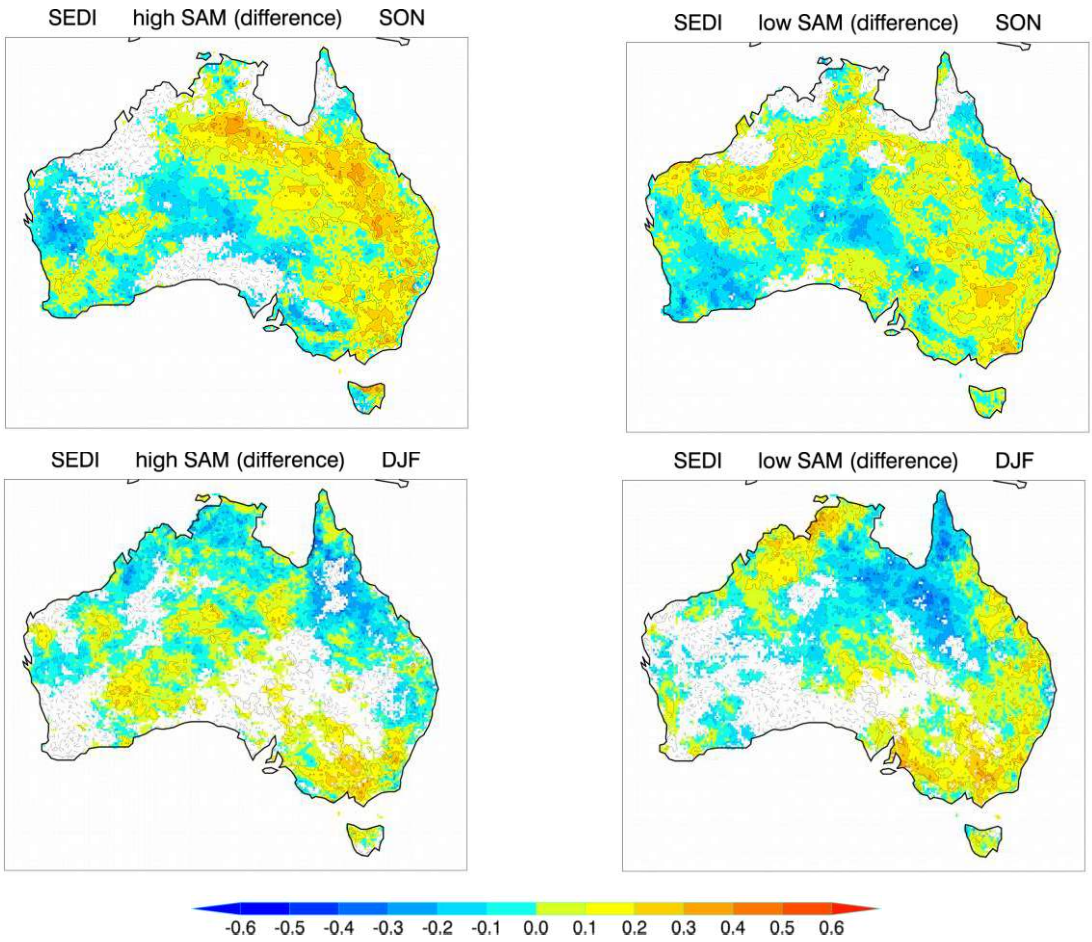

Figure 14: Same as Figure 12 but for the high (left column) and low (right column) SAM phase in SON (top row) and DJF (bottom row), shown as differences from when the SAM is weak.

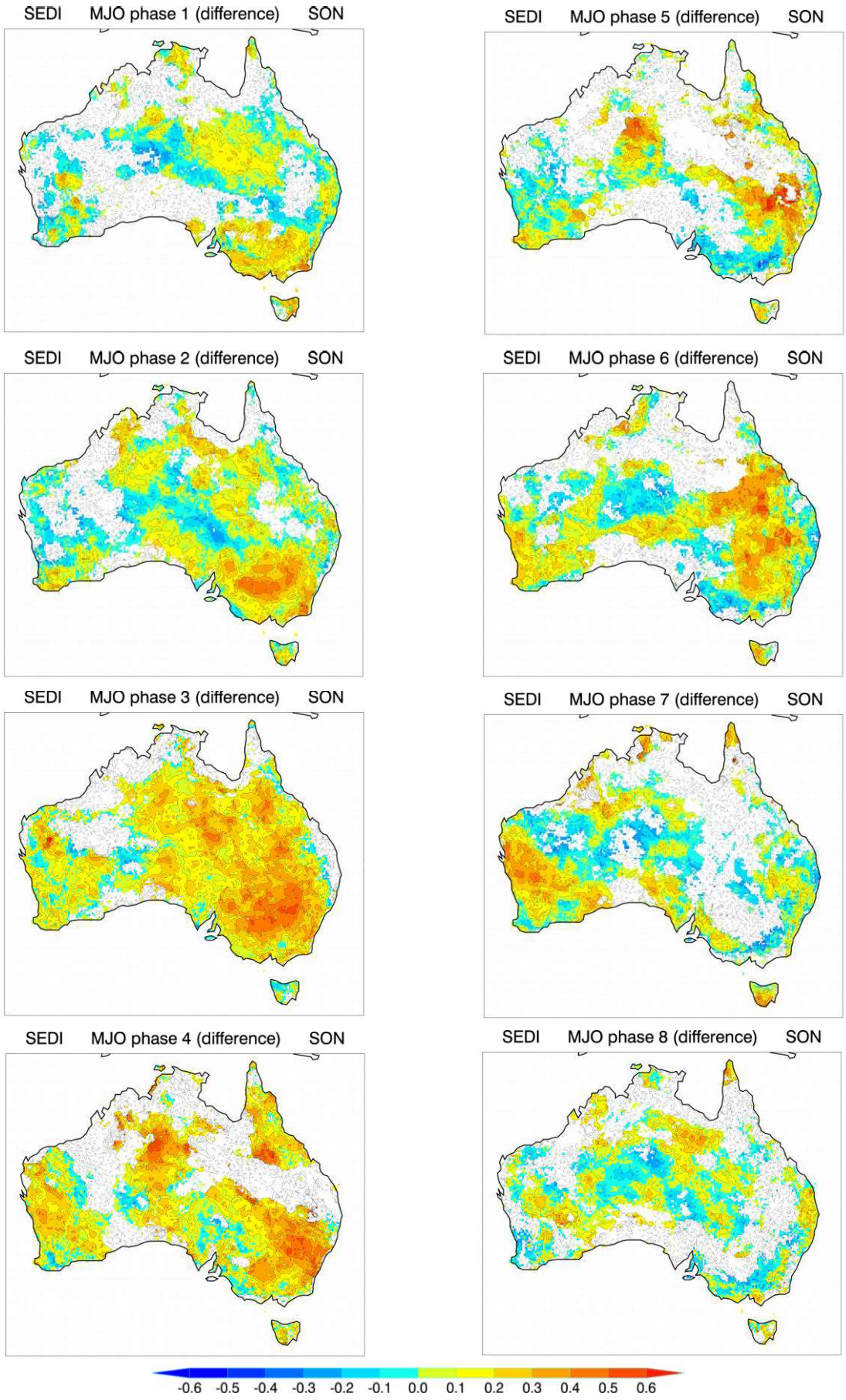

Figure 15: Same as Figure 12 but for MJO phases 1-8 in SON, shown as differences from when the MJO is weak.

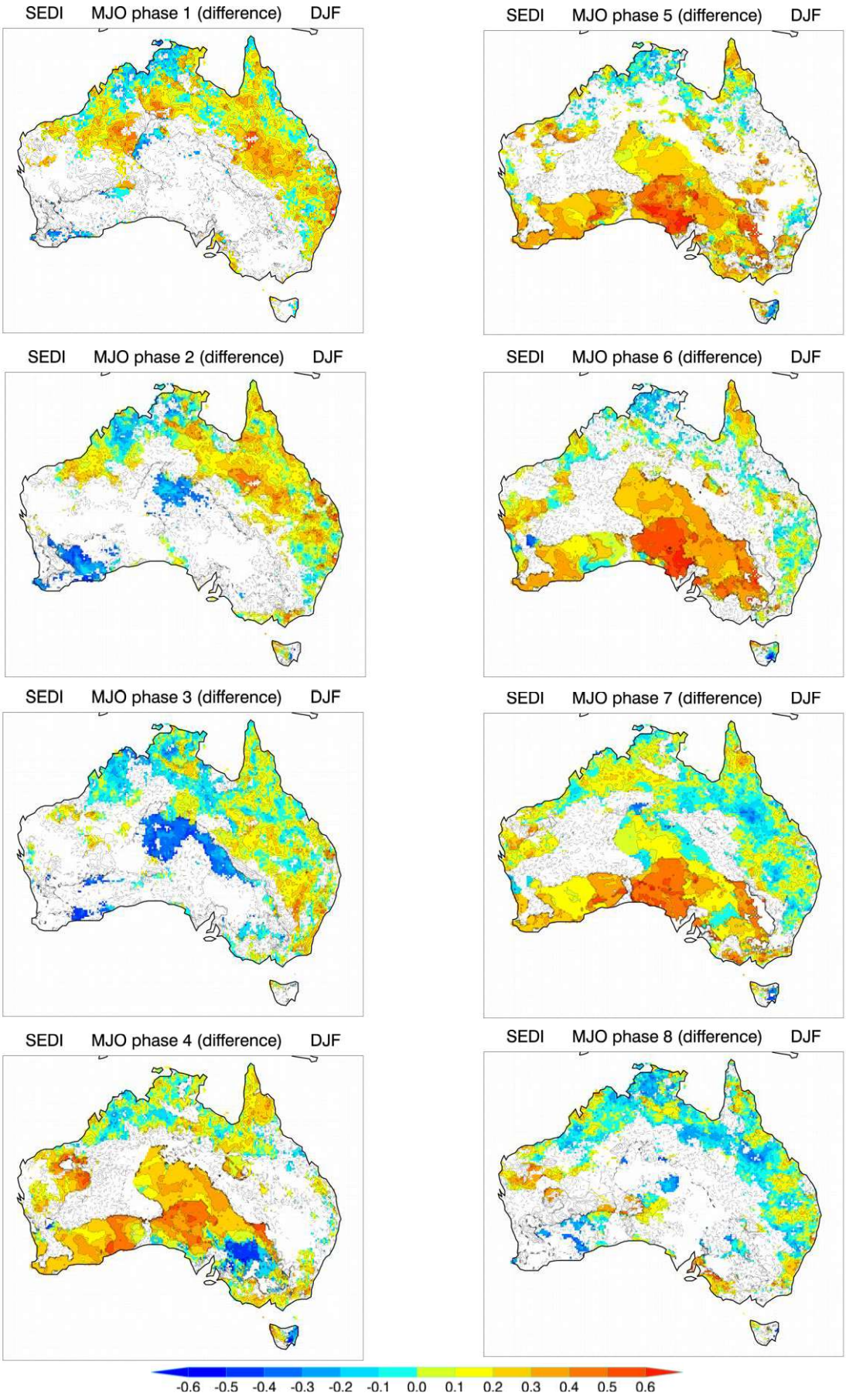

Figure 16: Same as Figure 12 but for MJO phases 1-8 in DJF, shown as differences from when the MJO is weak.

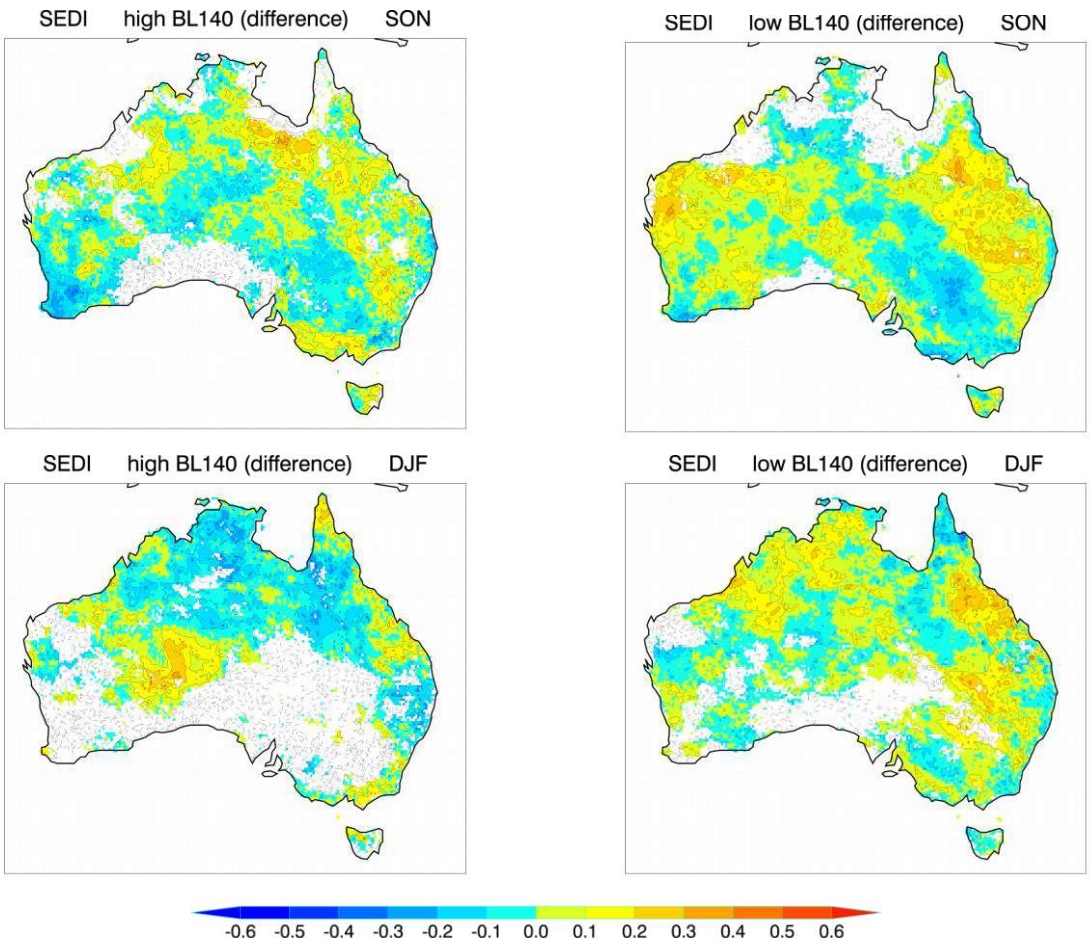

Figure 17: Same as Figure 12 but for high (left column) and low (right column) split-flow blocking activity at 140°E in SON (top row) and DJF (bottom row), shown as differences from when split-flow blocking activity is weak.

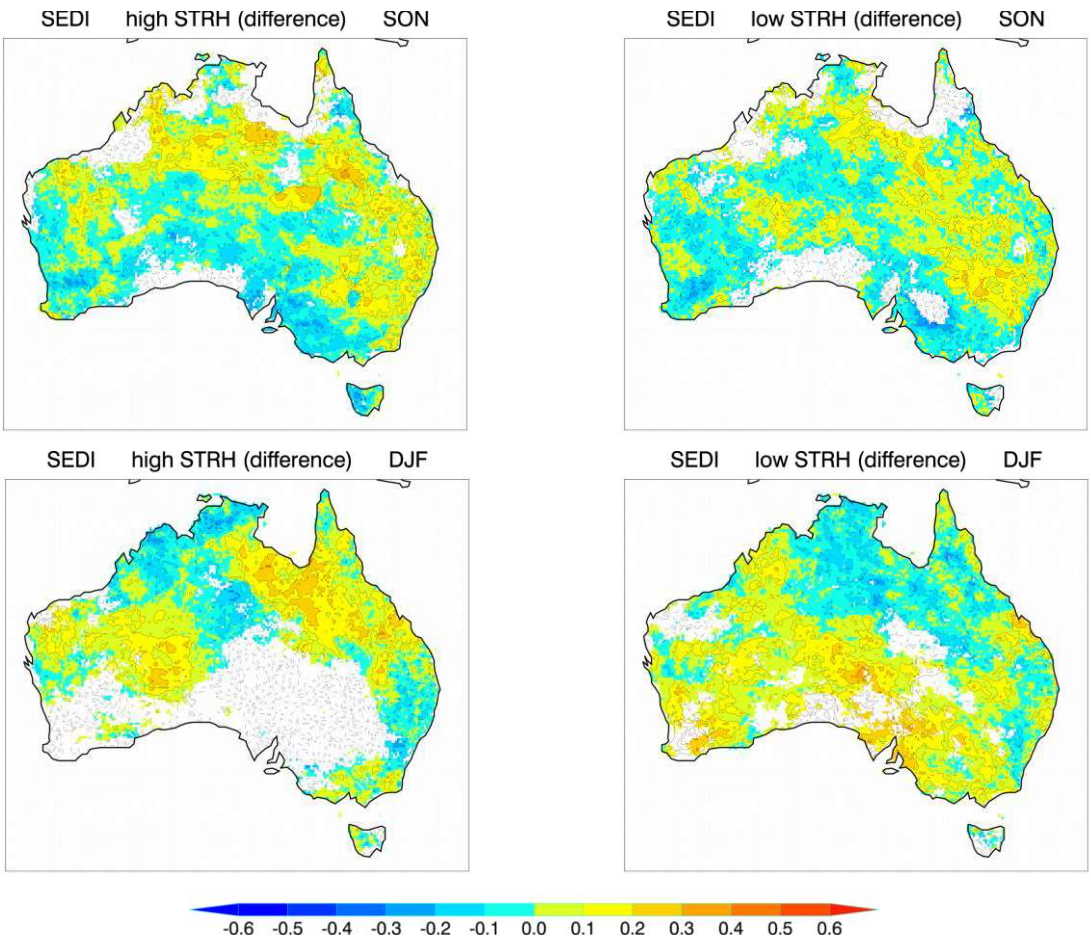

Figure 18: Same as Figure 12 but for high (left column) and low (right column) STRH activity in SON (top row) and DJF (bottom row), shown as differences from when STRH activity is weak.

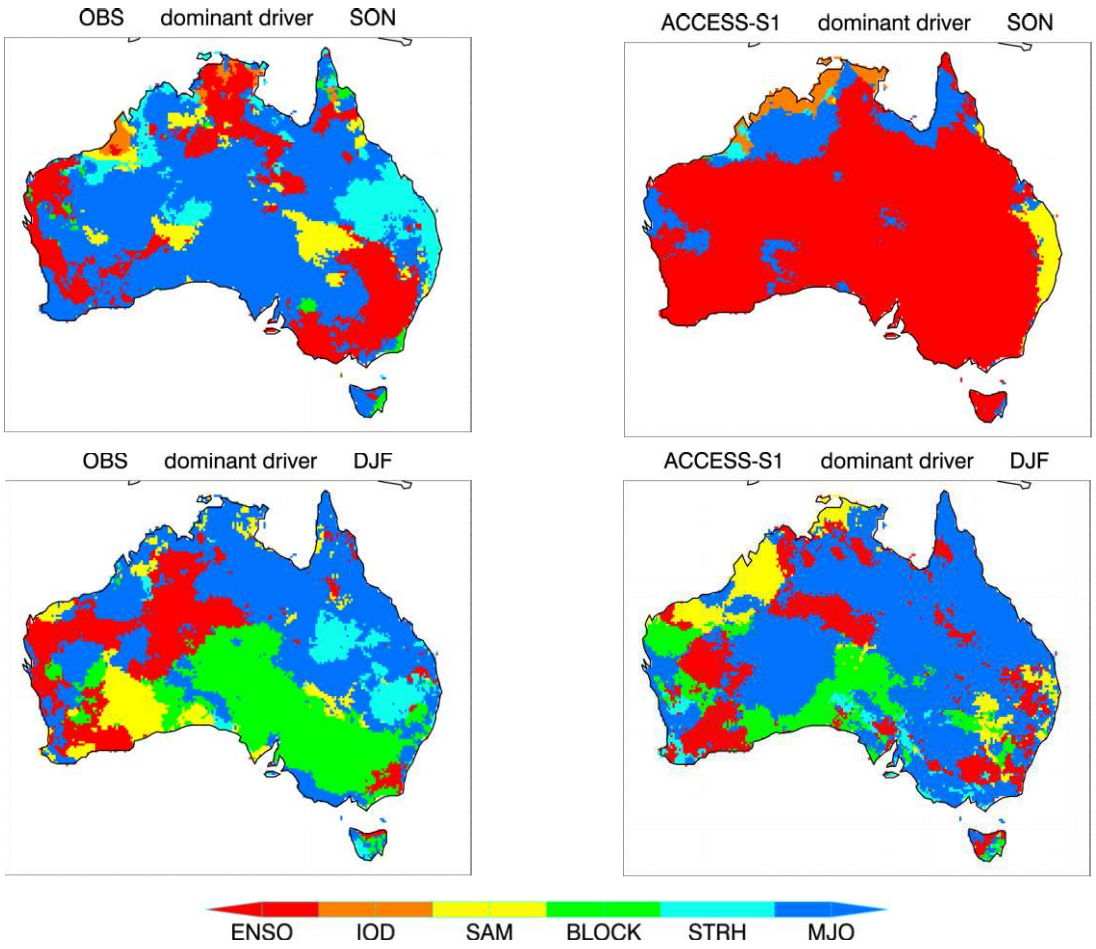

Figure 19: Each map shows the climate driver with the highest probability of upper decile weekly FFDI at each grid point in SON (top row) and DJF (bottom row), for observations (left column) and ACCESS-S1 at lead times of 2-3 weeks (right column).